



# Determination of the vertical distribution of in-cloud particle shape using SLDR-mode 35 GHz scanning cloud radar

Audrey Teisseire<sup>1</sup>, Patric Seifert<sup>1</sup>, Alexander Myagkov<sup>2</sup>, Johannes Bühl<sup>1</sup>, and Martin Radenz<sup>1</sup>

<sup>1</sup>Leibniz Institute for Tropospheric Research, Permoserstraße 15, 04318 Leipzig, Germany

<sup>2</sup>RPG Radiometer Physics GmbH, Werner-von-Siemens-Str. 4, 53340 Meckenheim, Germany

**Correspondence:** Audrey Teisseire (teisseire@tropos.de)

Received: 11 December 2022 – Discussion started: 12 January 2023

Revised: 11 December 2023 – Accepted: 18 December 2023 – Published: 12 February 2024

**Abstract.** In this study we present an approach that uses the polarimetric variable SLDR (slanted linear depolarization ratio) from a scanning polarimetric cloud radar MIRA-35 in the SLDR configuration, to derive the vertical distribution of particle shape (VDPS) between the top and base of mixed-phase cloud systems. The polarimetric parameter SLDR was selected for this study due to its strong sensitivity to shape and low sensitivity to the wobbling effect of particles at different antenna elevation angles. For the VDPS method, elevation scans from 90 to 30° elevation angle were deployed to estimate the vertical profile of the particle shape by means of the polarizability ratio, which is a measure of the density-weighted axis ratio. Results were obtained by retrieving the best fit between observed SLDR from 90 to 30° elevation angle and respective values simulated with a spheroidal scattering model. The applicability of the new method is demonstrated by means of three case studies of isometric, columnar, and plate-like hydrometeor shapes, respectively, which were obtained from measurements at the Mediterranean site of Limassol, Cyprus. The identified hydrometeor shapes are demonstrated to fit well to the cloud and thermodynamic conditions which prevailed at the time of observation. A fourth case study demonstrates a scenario where ice particle shapes tend to evolve from a pristine state at the cloud top toward a more isometric shape or less dense particles at the cloud base. Either aggregation or riming processes contribute to this vertical change of microphysical properties. The new height-resolved identification of hydrometeor shape and the potential of the VDPS method to derive its vertical distribution are helpful tools to understand complex processes such as riming or aggregation, which occur particularly in mixed-phase clouds.

## 1 Introduction

In the troposphere, a rich variety of cloud types exists, which are formed by characteristic microphysical processes. The structure of clouds is in general determined by the complex interaction of water vapor, ice, liquid droplets, vertical air motion, and aerosol particles, acting as cloud condensation nuclei (CCN) or ice nucleating particles (INP) (Pruppacher and Klett, 1997; Morrison et al., 2012; Ansmann et al., 2019). While in warm clouds the collision–coalescence process is the primary process responsible for the formation of precipitation, the situation is more complicated in ice-containing clouds having temperatures between  $-40$  and  $0^{\circ}\text{C}$ . In this temperature range, the coexistence of supercooled liquid water and ice is possible. Thus, in these mixed-phase clouds, multiple cloud microphysical processes are intertwined as they contain a three-phase colloidal system consisting of water vapor, ice particles, and supercooled liquid droplets (Korolev et al., 2017). The initial partitioning between the ice and liquid water is determined by the CCN and INP reservoir and represents the prevalent conditions for secondary ice formation processes, riming and aggregation (Solomon et al., 2018; Fan et al., 2017), which are greatly involved in the precipitation transition in mixed-phase clouds.

Observation of the hydrometeor habit is a possible way to study cloud formation and precipitation because particle shape can be considered a fingerprint of crucial processes, including crystal growth, evaporation rate, ice crystal fall speed, and cloud radiative properties (e.g., Avramov and Harrington, 2010). Shape allows us to distinguish pristine ice crystals from hydrometeors which have grown via aggregation or riming processes and can be considered as a tracer

of the different processes contributing to the evolution of a cloud system. The overall structure of ice crystals grown in air can be classified into plate-like and columnar shapes as a function of temperature between  $-40$  and  $0^{\circ}\text{C}$ . Bühl et al. (2016) and Myagkov et al. (2016a) showed that primary ice formation dominates in thin layers of stratiform or mixed-phase clouds of a geometrical thickness  $\leq 350\text{ m}$ , as growth processes in these thin clouds are constrained (Fukuta and Takahashi, 1999). In such cloud systems and conditions of liquid water saturation, the shape of ice crystals is thus related directly to the environmental temperature (Myagkov et al., 2016b). However, further complexity can be expected when the cloud systems become deeper and when the thermodynamic structure is less well defined as in single-layer stratiform mixed-phase clouds. Techniques which make it possible to detect the hydrometeor shape have great potential to contribute additional capabilities for the monitoring of cloud systems, to expand the understanding of the microphysical properties involved, and to support the improvement of the representation of these processes in numerical models. A way to discriminate different hydrometeor populations is the separation of peaks in cloud radar Doppler spectra (Radenz et al., 2019; Kalesse et al., 2019; Luke et al., 2021) using observations of ground-based cloud radar. However, this technique is limited, e.g., with respect to atmospheric turbulence, which broadens the spectra and makes the detection and separation of peaks difficult or even impossible. Moreover, hydrometeors with similar terminal fall velocities (e.g., drizzle and small ice) cannot be distinguished in the Doppler spectrum. In this case, it is possible to look at the Doppler spectra of polarimetric parameters such as linear depolarization ratio (LDR) or slanted linear depolarization ratio (SLDR) to confirm in which spectral mode the crystals are present.

Polarimetric cloud radar techniques have been shown to be valuable tools for the qualitative detection of ice crystal shape (Matrosov et al., 2001, 2005; Reinking et al., 2002). Matrosov et al. (2012) demonstrated an approach where they associated measurements of SLDR-mode scanning cloud radar with visual observations of ice crystal habits during a precipitation event. While their study demonstrates well the relationship between SLDR signatures and particle shape, it did not yet allow them to quantify the particle shape directly based on the measurements. Such an approach has been presented by Myagkov et al. (2016a), who succeeded in predicting the particle shape and orientation based on hybrid-mode scanning cloud radar observations by means of the two quantitative parameters – polarizability ratio and degree of orientation, respectively. Myagkov et al. (2016a) have shown that existing backscattering models, assuming the spheroidal approximation of cloud scatters, can be applied to establish a link between a set of measured polarimetric variables and the polarizability ratio. The polarizability ratio is a parameter defined by the geometric aspect ratio of particles and their refractive index. For ice particles the refractive index is almost

a linear function of their apparent ice density. Note, that it is not directly possible to infer the aspect ratio and the apparent ice density from the polarizability ratio. However, since the polarizability ratio depends on both variables, it can be used to track the evolution of the ice particles from pristine state to aggregates and rimed particles in observational studies. Polarizability ratio profiles are also valuable for modeling studies since the profiles can be used to constrain microphysical processes of ice growth. The first attempt to utilize polarizability ratios to improve ice characterization in models was recently made by Welss et al. (2023). Based on polarizability ratios the authors have updated the ice growth characterization for the explicit habit prediction in the Lagrangian super-particle ice microphysics model McSnow developed by the German Weather Service (DWD, Brdar and Seifert, 2018). Although developed for SLDR mode and simultaneous transmit simultaneous receive (STSR, hybrid)-mode cloud radars, the applicability of the shape and orientation estimation retrieval was originally demonstrated only for an STSR-mode scanning 35 GHz cloud radar, based on observations of stratiform cloud layers during the 1-month field campaign Analysis of Composition of Clouds with Extended Polarization Techniques (ACCEPT, Myagkov et al., 2016a).

Even though the number of scanning STSR-mode cloud radars has been continuously growing in Europe, a number of measurement sites within ACTRIS (the Aerosol, Clouds and Trace Gases Research Infrastructure) are equipped with scanning LDR radars (Madonna et al., 2013; Löhnert et al., 2015; Tetoni et al., 2022). Such radars can be modified to the SLDR mode with relatively small efforts and investments, and as a result can provide long-term observational datasets for retrieving the polarizability ratio of ice-containing clouds in different climatic zones. Therefore, the main goal of this study is to derive the vertical distribution of particle shape in clouds using the spheroidal scattering model developed by Myagkov et al. (2016a) for application to regular long-term observations of an SLDR-mode 35 GHz scanning cloud radar. We introduce a simplified and versatile version of the original STSR-mode approach by concentrating on the retrieval of the polarizability ratio, as we consider this parameter to be more relevant for the investigation of cloud microphysical processes in comparison to the degree of orientation. This paper aims at demonstrating the ability of the vertical distribution of particle shape (VDPS) method, to characterize particle properties using data with a newly configured SLDR-mode 35 GHz cloud radar which was deployed in the Cyprus Clouds, Aerosols and pRecipitation Experiment (CyCARE, Ansmann et al., 2019) field campaign in Limassol, Cyprus. We also illustrate that a profile of the derived polarizability ratio can be potentially used to detect microphysical processes affecting the evolution of ice particles in deep precipitating clouds. In Sect. 2, the instrumentation, campaign setup, and polarimetric parameter SLDR are described. The VDPS method is introduced in Sect. 3 and an evaluation of the VDPS method is presented in Sect. 4. Case

**Table 1.** Technical characteristics of MIRA-35 SLDR-mode cloud radar during the deployment in the CyCARE campaign in Limassol, Cyprus.

Parameters	Values
Pulse power	30 kW
Pulse length	208 ns
Pulse repetition frequency	7500 Hz
Elevation angle velocity	0.5 deg s <sup>-1</sup>
nFFT points	512
Number of range gates	498
Number of spectral averages	15
Integration time	1 s
Range resolution	31.18 m
Reflectivity sensitivity (1 s averaging at range = 5 km)	-48 dBZ
Co-cross-channel isolation	-35 dB

studies showing isometric particles, columnar crystals, and plate-like crystals will be discussed, and a fourth case study showing a transformation in shape of particles from the cloud top to the cloud base will be presented to demonstrate the potential of the VDPS method to detect and describe micro-physical transformation processes. In Sect. 5, we elaborate on the advantages and limits of this new algorithm as well as on possible future improvements.

## 2 Dataset

### 2.1 SLDR-mode 35 GHz cloud radar MIRA-35

The central instrument for the present study is a modified version of the 35 GHz cloud radar MIRA-35, which is operated in SLDR mode. MIRA-35 in general is a dual-polarization (LDR-mode) radar which emits linearly polarized radiation through the co-channel, while the returned signals are received in both the co- and cross-channels. The SLDR mode cloud radar was implemented based on the conventional linear depolarization ratio (LDR) mode by 45° rotation of the antenna system around the emission direction. While numerous polarimetric configurations of radar systems exist (Bringi and Chandrasekar, 2001, Chap. 6), the LDR mode is currently the most common one among cloud radars. The properties of the standard LDR mode MIRA-35 are elaborated in detail in Görsdorf et al. (2015). The technical characteristics of MIRA-35 used in the CyCARE campaign in Limassol, Cyprus, are given in Table 1.

Standard vertical-stare LDR-mode allows us only to discriminate between hydrometeors with an isometric intersection and with a columnar intersection (Bühl et al., 2016), i.e., aggregates cannot be separated from generally horizontally oriented plate-like particles in vertical-stare mode because their scattering intersections appear to be similar. In order to optimize the MIRA-35 cloud radar for improved measurements of hydrometeor shape and orientation, two modifications were applied to the standard setup as it is described by

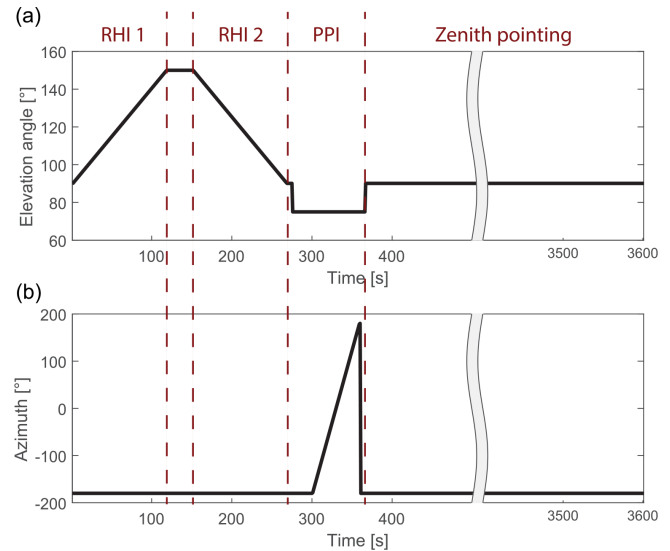


**Figure 1.** Temporal evolution of elevation angle (a) and azimuth angle (b) during the hourly scan cycle of SLDR MIRA-35 as applied during CyCARE. Dashed vertical red lines denote the time periods of the different RHI (range-height indicator), PPI (plan-position indicator), and zenith-pointing scan patterns.

Görsdorf et al. (2015). First, the cloud radar was mounted onto a positioner platform which allows for a freely definable position of the radar within a half sphere given by 360° of azimuth and 180° of elevation. The second modification addresses a 45° rotation of the antenna around the emission direction. This operation mode, in general defined as SLDR mode, has specific advantages in studies of the intrinsic relationship between the polarimetric signature of the particle shape and radar elevation angle. In contrast to the standard LDR mode, variations in the orientation of hydrometeors only have small effects on the measured SLDR, even at low elevation angles (Matrosov, 1991). In turn, SLDR in vertical pointing mode (elevation = 90°) is similar to the LDR observed with standard MIRA-35 systems. This behavior is also of advantage because it ensures direct comparability with other standard LDR-mode radars in vertical-pointing measurements. In the framework of the present study, the radar was steered toward geographic south direction (180° azimuth angle) and performed range-height indicator (RHI) scans from 90° (zenith-pointing) to 150°, corresponding to 30° elevation over the horizon toward north direction. This notation of the elevation angle range will be used throughout this article and figures.

Figure 1 describes the setup of one scan cycle as it was applied in the measurements of the SLDR mode MIRA-35, used in this study. Each scan cycle starts at minute 29 of each hour. Within 6.5 min, two RHI scans from 90 to 150° and from 150 to 90° elevation angle and one plan-position indicator (PPI) scan at 75° elevation are performed. During the remaining 53.5 min of each measurement hour, vertical-

stare observations (at 90° elevation angle) are performed to support standard retrievals, such as done within Cloudnet (Illingworth et al., 2007; Radenz et al., 2021) or as required for Doppler-spectra analysis techniques (Radenz et al., 2019; Bühl et al., 2019; Vogl et al., 2022; Schimmel et al., 2022). A limit of 150° elevation angle was established to avoid physical barriers such as trees or buildings. It is also a reasonable compromise between the required horizontal homogeneity and the intensity of the SLDR gradient produced by the observed hydrometeors. As the detailed procedure of data acquisition was depicted by Görsdorf et al. (2015) and Myagkov et al. (2016b), the determination of the polarimetric parameters required for this study is only briefly outlined below. The primary measurement parameters are thus the Doppler power spectra received by the detectors in the co- and cross-channels with respect to the emitted polarization plane  $P_{\text{co}}(\omega_k)$  and  $P_{\text{cx}}(\omega_k)$ , respectively, with  $\omega_k$  being the Doppler frequency shift of each individual spectral component  $k$ . The herein presented VDPS method only considers the main peak of the detected Doppler spectrum in the co-channel. Thus, in a next step, each data point is screened for the spectral component  $\omega_k^{\text{max}}$  where  $P_{\text{co}}(\omega_k)$  is maximal. The following parameter is then only calculated for the Doppler spectral bin  $\omega_k^{\text{max}}$ . The frequency dependency is thus omitted in the following and the polarimetric properties linear depolarization ratio in slanted mode (SLDR) can be derived as follows:

$$\text{SLDR} = \frac{\langle P_{\text{cx}} \rangle}{\langle P_{\text{co}} \rangle}, \quad (1)$$

where  $\langle \rangle$  denotes averaging over a number of collected Doppler spectra.

The raw spectra of the signal-to-noise ratio (SNR) are subject to noise artifacts. Correspondingly, a noise filtering is performed to remove values which are below a given threshold value

$$n = m + 3\sigma, \quad (2)$$

with  $m$  being the mean and  $\sigma$  being the standard deviation of noise in the co-channel. The properties of the noise in the co-channel are estimated from the last five range gates of each profile assuming no scattering is present. A spectral line with the power in the cross channel below  $n$  is excluded from the following analysis.

An important technical aspect which needs to be considered in the data analysis is the leakage of a fraction of signal from the co-channel into the cross-channel. The co-cross-channel isolation was determined with the experimental approach described by Myagkov et al. (2015), by means of identification of the minimum SLDR value that was measured at zenith-pointing, in the presence of light drizzle. The co-cross-channel isolation used in this study was thus found to be  $-35$  dB with MIRA-35.

## 2.2 Dataset

MIRA-35 is operated as part of the Leipzig Aerosol and Cloud Remote Observations System (LACROS, Radenz et al., 2021), a suite of ground-based instruments of the Leibniz Institute for Tropospheric Research (TROPOS). Besides the SLDR-mode Ka-band scanning cloud radar, LACROS comprises an extensive set of active and passive remote sensing instruments for the characterization of aerosol properties, clouds, and precipitation, including multi-wavelength polarization lidar, Doppler lidar, microwave radiometer, and optical disdrometer. Data used in this study were acquired in the framework of a deployment of LACROS at the Mediterranean site of Limassol, Cyprus (34.68° N, 33.04° E, 10 m a.s.l.) during the CyCARE field campaign (Ansmann et al., 2019; Radenz et al., 2021). The region of Cyprus is a relevant location for studies of the impact of aerosol on cloud processes because of a large variety of air pollutants, desert dust, and marine salt particles in the atmosphere above the island. The CyCARE campaign was conducted from September 2016 to March 2018 and aimed at the determination of the relationship between aerosol properties and the formation of cirrus and mixed-phase clouds (Ansmann et al., 2019; Radenz et al., 2021) in the heterogeneous freezing regime.

## 2.3 Measured SLDR and modeled $\widehat{\text{SLDR}}$

The VDPS method combines simulations of  $\widehat{\text{SLDR}}$  (thereby and hereafter, the symbol  $\hat{\phantom{x}}$  denotes simulated parameters) with measurements of SLDR (see Sect. 3). The study is based on the same set of equations as was previously presented by Myagkov et al. (2016a). The theoretical framework assumes Rayleigh scattering and utilizes a spheroidal approximation of particle shape (Matrosov, 1991). In the scattering model used, polarimetric variables depend on two parameters: the polarizability ratio  $\xi$ , which describes the particles by means of a density-weighted axis ratio, and the degree of orientation  $\kappa$ , which is a measure of the preferred orientation of the spheroids population. It is well known that the Rayleigh approximation is not always applicable to simulate scattering from individual and large ice particles at wavelengths shorter than C-band, which holds especially for absolute values such as reflectivity factor (Lu et al., 2016). At shorter wavelengths, the direct dipole approximation (DDA, Draine and Flatau, 1994) can be used to simulate scattering of individual ice particles having a complex shape. Meanwhile, extensive databases exist (Lu et al., 2016) and have found, e.g., special attention already for the application of multi-wavelength radar studies (von Terzi et al., 2022). However, these simulations and associated studies are often limited to a number of predefined shapes and therefore do not necessarily represent the realistic distribution of ice particles observed by a radar (Leinonen et al., 2018). Simulations for a single particle also do not reflect the volumetric scattering effects of a large population of hydrometeors. In general, ice particles

in a scattering volume have arbitrary shapes and the contribution of individual particles to the backscattering radar observables and especially polarimetric quantities is averaged out (Matrosov, 2021; von Terzi et al., 2022). We decided to assume the Rayleigh scattering and the spheroidal particle approximation (Matrosov, 1991; Ryzhkov, 2001; Bringi and Chandrasekar, 2001) because (1) such a model explains general polarimetric scattering effects with just a few parameters (axis ratio, permittivity, and canting angle), (2) the model parameters are well constrained by the observations, (3) the volumetric scattering is taken into account, and (4) the model enables a computationally effective derivation of the polarizability ratio. In this study, we sort particles into three primary categories based on their shape: oblate particles, which have a polarizability ratio less than 1, prolate particles, characterized by a polarizability ratio greater than 1, and isometric particles, where the polarizability ratio ranges from 0.8 to 1.2, depending on the radar calibration (see Table 2). With respect to the definition in this study, we consider particles as isometric when they do not produce considerable polarimetric signatures. Such particles have either spherical or just slightly non-spherical shape. In the case of particles with a low refractive index (i.e., low permittivity), their reduced response to radar waves may lead to scattering characteristics that resemble those of isometric particles.

Figure 2 shows the dependencies of  $\widehat{\text{SLDR}}$  on the polarizability ratio and degree of orientation of ice particles at  $90^\circ$  (zenith) and  $150^\circ$  ( $60^\circ$  off-zenith) elevation angle. Figures 2a and b show that  $\widehat{\text{SLDR}}$  is mostly sensitive to  $\xi$  (as noted by Matrosov et al., 2001), which demonstrates the relevance of using SLDR rather than Differential Reflectivity (ZDR) to determine the particle shape. For our radar configuration, the realistic range of possible polarizability ratios  $\xi$  spans from 0.3 to 2.3 and the degree of orientation  $\kappa$  ranges from  $-1$  to  $1$ .  $\kappa$  will only be briefly elaborated in this section as it will be used only qualitatively in the frame of this study. In the case of spheroidal approximation and Rayleigh scattering regime, the polarizability ratio  $\xi$ , describing the shape of particles, is a function of permittivity and axis ratio and is independent of the particle volume. A polarizability ratio  $\xi = 1$  designates spherical particles or particles with low density, while  $\xi < 1$  and  $\xi > 1$  describe oblate and prolate particles, respectively. Also for non-isometric particles, a decrease in apparent particle density causes  $\xi$  to approach a value of unity (Myagkov et al., 2016a). The degree of orientation characterizes the width of the particle orientation angle distribution (the degree of orientation is explained in more detail in Myagkov et al. (2016a), in their Fig. 9 and Eq. (11)). For instance,  $|\kappa| = 0$  corresponds to uniform distribution, while  $|\kappa| = 1$  indicates that all particles are aligned in the same way. The sign of  $\kappa$  indicates the preferable orientation of the symmetry axis, i.e.,  $\kappa = +1$  indicates that all particles are aligned and have a vertical symmetry axis,  $\kappa = -1$  corresponds to the case when particles have a predominantly horizontally aligned symme-

try axis. We therefore assume  $\kappa \geq 0$  for oblate particles and  $\kappa \leq 0$  for prolate particles. Regarding Fig. 2a and b we consider that  $\kappa \approx -0.3$  corresponds to randomly oriented isometric particles when SLDR is minimal and these values do not depend on the elevation angle (Myagkov et al., 2016a).

A subset from Fig. 2 is presented in Fig. 3 in order to demonstrate the general, idealized relationship between  $\widehat{\text{SLDR}}$  and elevation angle for the main particle shape classes oblate (“+”), isometric (“o”), and prolate (“-”), thereby assuming predominantly horizontal orientation. Indeed, the “+” symbol is located in the oblate domain (zone A) described by a polarizability ratio  $\xi = 0.35$  and a degree of orientation  $\kappa = 0.85$  representing horizontally oriented plate-like particles, while the “\*” symbol is located in the prolate domain (zone B) described by  $\xi = 2.15$  and  $\kappa = -0.85$  representing horizontally oriented columnar crystals. The symbol “o” is determined by  $\xi = 1$  and  $\kappa = -0.4$ , such as randomly oriented spherical particles like liquid droplets (Myagkov et al., 2016a), which is representative for the isometric domain (zone C). A value of  $\widehat{\text{SLDR}}$  is derived for all elevation angles from  $90$  and  $150^\circ$ , leading to Fig. 3, which links our study to findings of Matrosov et al. (2012) showing distinct elevation-dependent signatures of SLDR for particles with different shapes. As illustrated in Fig. 3, prolate particles are characterized by nearly constant and relatively high values of SLDR at all elevation angles, which reach values of around  $-25$  dB for solid columns and more than  $-20$  dB for pronounced needles of high-axis ratio (Reinking et al., 2002; Matrosov et al., 2012). The isometric primary particle shape class is represented by constantly low values of SLDR at all elevation angles between  $90$  and  $150^\circ$ . Finally, plate-like particles, belonging to the oblate particle class, known to align predominantly horizontally along their planar planes, produce scattering similar to isometric particles observed at zenith-pointing ( $90^\circ$  elevation angle) and will increasingly appear oblate at low elevation angles. That is why in the case of plate-like hydrometeors, SLDR, representative of the particle shape, is minimal at zenith-pointing and increases from  $90$  to  $150^\circ$  elevation angle. Indeed, at zenith-pointing, plate-like crystals have random orientation in the polarization plane, while at a low elevation angle horizontally aligned particles produce rather coherent returns in both polarimetric channels. Note that it is not directly possible to classify the type of isometric particles (e.g., aggregates or rimed particles can be isometric particles, too) since they have similar angular polarimetric signatures at all elevation angles. Discrimination between these types of particles can be made, e.g., using multiple-frequency observations (Kneifel et al., 2016) but this is out of the scope of the current study. The VDPS method aims to differentiate the three main particle shape classes and their vertical evolution within cloud systems in order to determine microphysical processes occurring in mixed-phase clouds.

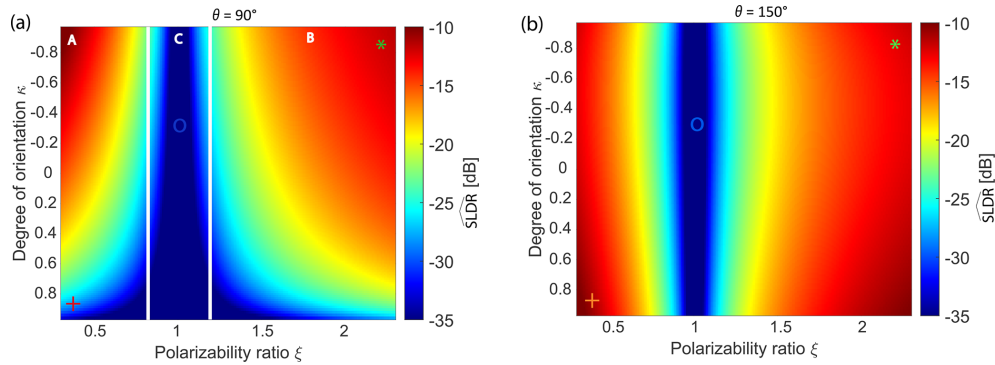


**Figure 2.** Modeled  $\widehat{\text{SLDR}}$  as a function of polarizability ratio  $\xi$  and degree of orientation  $\kappa$  for particles at (a)  $\theta = 90^\circ$  and (b)  $\theta = 150^\circ$  antenna elevation angle. “+” (oblate particles), “O” (isometric particles) and “\*” (prolate particles) symbols are data points used in Fig. 3. The elevation dependency of these three scenarios is depicted further in Sect. 2.3. The two vertical white lines in (a) separate the three particle domains of oblate (zone A), prolate (zone B), and isometric (zone C) hydrometeors.

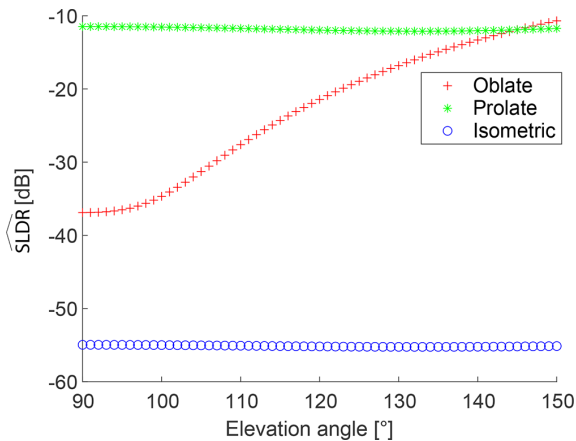


**Figure 3.** Distributions of modeled  $\widehat{\text{SLDR}}$  as a function of elevation angle between 90 and 150° for typical horizontally oriented oblate (“+” red), isometric (“o” blue), and prolate (“\*” green) particles, respectively. The same symbols in Fig. 2 illustrate the location of the data points in the model field at 90° (Fig. 2a) and 150° (Fig. 2b) elevation angle.

### 3 Methodology

The concept of the VDPS approach is to realize a tailored retrieval of the vertical distribution of particle shape. The VDPS method, adapted for the SLDR-mode scanning cloud radar as introduced in Sect. 2.1, has the particularity of combining simulated and measured values of SLDR at only two elevation angles, isolated from a full RHI scan.

As the VDPS method relies on polarimetric measurements at different elevation angles, horizontal homogeneity of the observed clouds is required. The scale of the horizontal homogeneity is defined by the maximum observation distance of the cloud radar used and the lowest elevation angle (10–15 km and 30°, respectively). Thus, the required scale of the horizontal homogeneity is mostly below 13 km, which is

comparable, e.g., to a footprint of a space-borne passive microwave sensor. A majority of stratiform clouds have much larger spatial scale. In addition, the algorithm requires a minimum number of data points in each layer, representing 15% of the total number of data points, as will be explained in Sect. 3.1.

The general flow chart describing the three-step procedure is depicted in Fig. 4. In the first step, presented in Sect. 3.1, the dataset is prepared for the evaluation against the spheroidal scattering model in Sect. 3.2. By combination of  $\widehat{\text{SLDR}}$  simulated by the spheroidal scattering model with SLDR observations, the range of possible primary particle shape classes is identified and the associated uncertainties are assessed in Sect. 3.2. In the final step presented in Sect. 3.3, linear regressions of SLDR vs. elevation angle are calculated and deployed to identify the correct primary particle shape class and to assign the proper polarizability ratio  $\xi$  from the set of possible solutions determined in Sect. 3.2.

#### 3.1 Determination of SLDR at the boundaries of the elevation range

For each of the four individual scan patterns described in Fig. 1, the returned signals in the co- and cross-channel  $P_{\text{co}}(\omega_k)$  and  $P_{\text{cx}}(\omega_k)$ , respectively, collected by MIRA-35 are saved in a level-0 file, in the pdm format defined by the company Metek. Consequently, the pdm data are in a first step converted into NetCDF format containing the polarimetric measurements of  $\text{SLDR}(\omega_k)$ , calculated with Eq. (1), as well as elevation angle and range. Next, the noise filtering (Eq. (2)) is applied as explained in Sect. 2.3 and only the maximum spectral component of the remaining noise-free spectra is selected. Thus, arrays containing one value of SLDR per elevation angle are obtained for each granule of time and range. All range values are converted into height above ground, using the elevation angle  $\theta$  as additional input. The VDPS algorithm runs automatically for each RHI



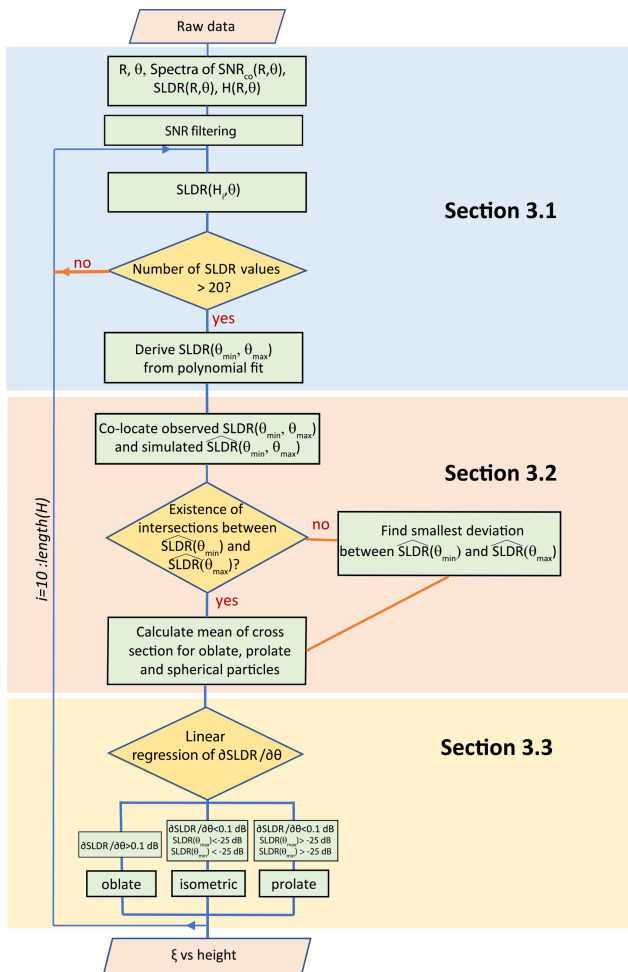


Figure 4. Flowchart describing the VDPS method.

scan selected. A main loop is used to separate the observations into multiple vertical “height” layers. In general, any arbitrary value of height resolution can be chosen. For the current study, each height step corresponds to the range resolution of MIRA-35 (31.18 m, i.e., the height resolution at zenith-pointing), as was done by Myagkov et al. (2016a). The following procedure is performed for each height layer which contains at least 20 values of SLDR from a full RHI scan recorded from 90° to 150° elevation angle (Fig. 1). The value of 20 points per layer represents about 15 % of the maximal number of data points. If this limit is not reached, it could mean that no cloud was detected at this layer or that not enough particles are contained at the investigated height level of the cloud, which would influence the quality of results. In this situation, the procedure will be stopped only for this layer at this step (no results are produced) and will continue to iterate into the next layer. If a sufficient number of data points was found at a height level, a new vector of  $SLDR(H, \theta)$  is built. The elevation range of  $SLDR(H, \theta)$  does not necessarily span the full elevation range of the RHI

scan, as some data points at the elevation limits might have been removed.

As shown in Fig. 3 and as will be elaborated on further in Sect. 3.3, polarimetric signatures of different particle shapes are most visible when the elevation angle difference of the performed scans is large. For this reason, a full RHI scan is used to verify the homogeneity of the investigated cloud (Sect. 3.1) and to calculate the SLDR linear regression (Sect. 3.3), but only values of SLDR at two elevation angles are needed in the model output (Sect. 3.2). In order to prepare the observational input for the evaluation against the spheroidal scattering model to be described in Sect. 3.2, we will look for the data points of SLDR associated with the smallest observed value of elevation angle ( $\theta_{min}$ , usually zenith-pointing) and to the largest value of elevation angle ( $\theta_{max}$ , usually 150°). Thus, in a next step, fit values of measured SLDR at the minimum elevation angle ( $SLDR(\theta_{min})$ ) and at maximum elevation angle ( $SLDR(\theta_{max})$ ) are calculated. These notations will be used further in Sect. 3.2. It can be seen in Fig. 3, that the relationship between SLDR and the elevation angle is not linear for SLDR, especially in the case of oblate particles, and the more appropriate method to calculate  $SLDR(\theta_{min})$  and  $SLDR(\theta_{max})$  for all cases is to use a 3<sup>rd</sup> degree polynomial fit.  $SLDR(\theta_{min})$  and  $SLDR(\theta_{max})$  are determined with the fit values from the 3<sup>rd</sup> degrees polynomial fit at  $\theta_{min}$  and  $\theta_{max}$ , respectively. As an example, Fig. 5 shows the distribution of SLDR from  $\theta_{min}$  to  $\theta_{max}$ . Values of  $SLDR(\theta_{min})$  and  $SLDR(\theta_{max})$  are readable at 90° ( $\theta_{min}$ ) and 150° ( $\theta_{max}$ ) elevation angle as  $SLDR(\theta_{min}) = -32$  dB and  $SLDR(\theta_{max}) = -11$  dB.  $SLDR(\theta_{min})$  and  $SLDR(\theta_{max})$  are saved and will be utilized in Sect. 3.2 for the evaluation against the spheroidal scattering model compiled at the same elevation angles  $\theta_{min}$  and  $\theta_{max}$ .

### 3.2 Estimation of the polarizability ratio for each layer

In the first step of the VDPS retrieval we find two SLDR values corresponding to  $\theta_{min}$  and  $\theta_{max}$  (Sect. 3.1). In the second step we search for values of the polarizability ratio and the degree of orientation for which the simulated  $\widehat{SLDR}$  fits to  $SLDR(\theta_{min})$  and  $SLDR(\theta_{max})$ .

The original spheroidal scattering model based on Myagkov et al. (2016a) does not take into account hardware-related effects and, therefore, predicts minimum values of  $\widehat{SLDR}$  that cannot be reached with the current radar technology due to the polarimetric coupling in the antenna system. The polarimetric coupling (co-cross-channel isolation) of the radar used is  $-35$  dB, as mentioned in Sect. 2.1, and leads to an increased uncertainty of the retrieval for particles with polarizability ratio between 0.9 and 1.1. The modeled distribution of  $\widehat{SLDR}$  from 90 to 150° elevation angle for three exemplary particle habits oblate, isometric, and prolate is illustrated in Fig. 3. This graphic represents the theoretical

relationship between  $\widehat{\text{SLDR}}$  and elevation angle in the three different primary particle shape classes, which is about to be faced with the direct measurements of SLDR. In the second part of this section, we compare the modeled  $\widehat{\text{SLDR}}$  and measured SLDR obtained from the polynomial fit (Sect. 3.1) at elevation angles  $\theta_{\min}$  and  $\theta_{\max}$ , as explained in Sect. 3.1. In order to consider potential measurement inaccuracies, the 95 % confidence interval  $\Delta_{95}$  of the polynomial fit will be used to determine the potential range of the intersection. The confidence interval is calculated as follows:

$$\Delta_{95} = 2\Delta, \quad (3)$$

where  $\Delta$  is the standard deviation of the difference between the measured and simulated values of SLDR at all available elevation angles from 90 to 150°. The model is processed at  $\theta_{\min}$  and  $\theta_{\max}$  and the algorithm identifies isolines of  $\widehat{\text{SLDR}}(\theta_{\min}) = \widehat{\text{SLDR}}(\theta_{\min}) \pm \Delta_{95}$ , and  $\widehat{\text{SLDR}}(\theta_{\max}) = \widehat{\text{SLDR}}(\theta_{\max}) \pm \Delta_{95}$ , in the modeled fields of  $\widehat{\text{SLDR}}$  at  $\theta_{\min}$  and  $\theta_{\max}$ , respectively. For example, in Fig. 6a and b we can see the isoline where  $\widehat{\text{SLDR}}(\theta_{\min}) = \widehat{\text{SLDR}}(\theta_{\min})$  plotted in red and the isoline where  $\widehat{\text{SLDR}}(\theta_{\max}) = \widehat{\text{SLDR}}(\theta_{\max})$  plotted in blue on the model, respectively. The two isolines are plotted together in Fig. 6c, highlighting intersections between  $\widehat{\text{SLDR}}(\theta_{\min})$ , shown as a red curve, and  $\widehat{\text{SLDR}}(\theta_{\max})$ , shown as a blue curve, resulting in  $\xi = 0.45$  and  $\xi = 2$ . If no intersection is found between  $\widehat{\text{SLDR}}(\theta_{\min})$  and  $\widehat{\text{SLDR}}(\theta_{\max})$ , the algorithm searches for the point where the difference between  $\widehat{\text{SLDR}}(\theta_{\min})$  and  $\widehat{\text{SLDR}}(\theta_{\max})$  is the lowest. Finally, the algorithm characterizes the  $x$ -axis positions (polarizability ratio  $\xi$ ) by deriving the mean and standard deviation of all overlapping data points included in each intersection between the isolines of  $\widehat{\text{SLDR}}(\theta_{\min})$  and  $\widehat{\text{SLDR}}(\theta_{\max})$  (Fig. 6). Three values of  $\xi$  are saved at each height iteration corresponding to the three primary particle shape classes: the first intersection in the oblate particle shape class with  $\xi < 1$  ( $\xi = 0.45$  in Fig. 6c), the second intersection for the prolate particle shape class with  $\xi > 1$  ( $\xi = 2$  in Fig. 6c), and a mean of these two intersections for the isometric or low-density particle shape class with  $\xi \approx 1$ . The procedure could be repeated in a similar manner for determination of the possible  $y$ -axis values, which are the possible solutions of the degree of orientation  $\kappa$ , which is, however, not in the scope of our study.

### 3.3 Identification and quantification of the primary particle shape class

The last step of the VDPS method consists of the identification of the primary particle shape class among the three possible solutions introduced in Sect. 3.2 and to quantify the primary particle shape class with the assigned value of  $\xi$ . As introduced in Sect. 2.3, the relationship between SLDR and the elevation angle is an important aspect to determine the particle shape (Reinking et al., 2002; Matrosov et al.,

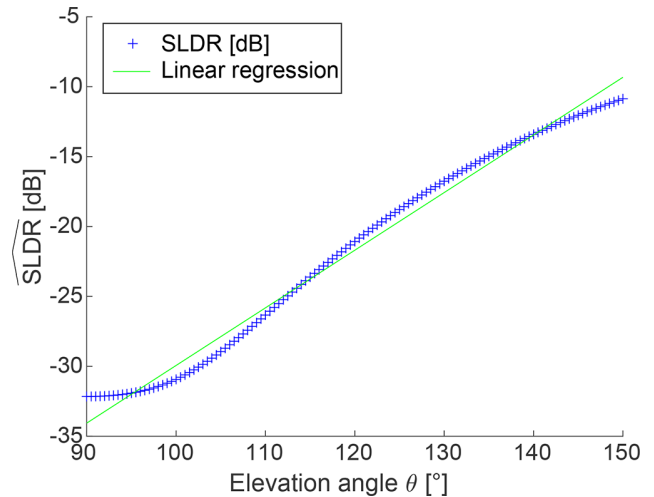


**Figure 5.** Distribution of SLDR as a function of elevation angle between  $\theta_{\min} = 90^\circ$  and  $\theta_{\max} = 150^\circ$  for the same dendritic crystal population as presented in Fig. 6:  $\text{SLDR}(\theta_{\min}) = -32$  dB,  $\text{SLDR}(\theta_{\max}) = -11$  dB, and  $\kappa = 0.85$ . The green line represents the SLDR linear regression calculated in Sect. 3.3.

2005, 2012) and will be used in the following to discriminate between the primary particle shape classes. A threshold of  $\frac{\partial \text{SLDR}}{\partial \theta}$  is determined in such a way that an unambiguous separation of the prolate, oblate, and isometric hydrometeor shape classes is possible, by applying a robust linear fit to all observed pairs of SLDR and elevation angle. The resulting limit values were derived to be  $\text{lim}_{\text{SLDR}} = 0.1$  dB deg<sup>-1</sup>, as a threshold describing a certain change of the SLDR in dB per degree of elevation angle, and  $\text{lim}_{\text{pro}} = -25$  dB, which describes the maximum value of SLDR to be associated to the prolate shape class. It should be noted that the two limit values might depend on the individual radar calibration. The actual shape class selection criteria are summarized in Table 2 and are described in the following. If the linear regression  $\frac{\partial \text{SLDR}}{\partial \theta}$  exceeds  $\text{lim}_{\text{SLDR}}$ , particles are assigned to the oblate primary particle shape class. If  $\frac{\partial \text{SLDR}}{\partial \theta}$  does not exceed  $\text{lim}_{\text{SLDR}}$  and if  $\text{SLDR}(\theta_{\min})$  and  $\text{SLDR}(\theta_{\max})$  exceed  $\text{lim}_{\text{pro}}$ , particles are assigned to the prolate primary particle shape class. If  $\frac{\partial \text{SLDR}}{\partial \theta}$  does not exceed  $\text{lim}_{\text{SLDR}}$  and if  $\text{SLDR}(\theta_{\min})$  and  $\text{SLDR}(\theta_{\max})$  are below  $\text{lim}_{\text{pro}}$ , particles are associated to the isometric primary particle shape class. If particles are assigned to the isometric particle shape class,  $\xi$  will be calculated as the mean of the associated values of  $\xi$  contained in both intersections of  $\widehat{\text{SLDR}}(\theta_{\min})$  and  $\widehat{\text{SLDR}}(\theta_{\max})$  on both sides of  $\xi = 1$  (Sect. 3.2). In the oblate and prolate primary particle shape classes, the error bars are calculated based on the intersections of the standard deviation obtained for  $\widehat{\text{SLDR}}(\theta_{\min})$  and  $\widehat{\text{SLDR}}(\theta_{\max})$ , following the same procedure as explained in Sect. 3.2. Concerning the isometric primary particle shape class,  $\xi$  values of the two intersections identified before are used as error bars. Figure 5 depicts the relationship between SLDR and elevation angle from  $\theta_{\min}$  to



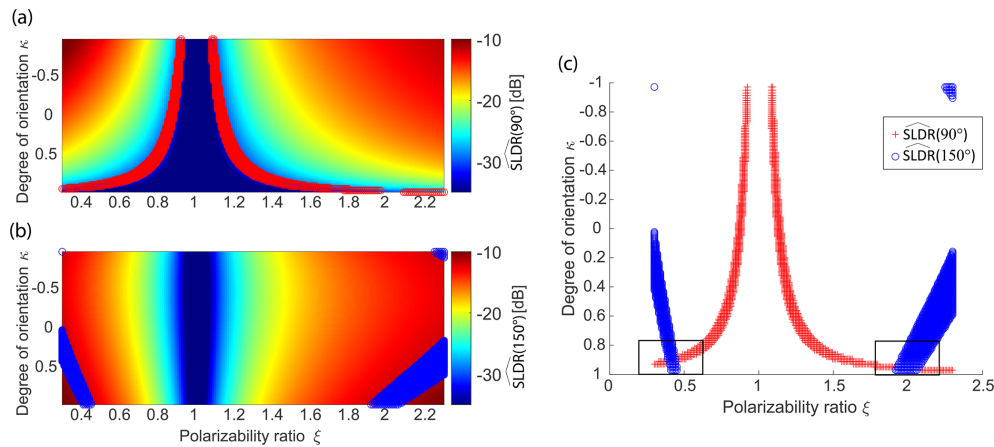


**Figure 6.** Determination of the possible values of  $\xi$  by searching for the intersections between  $\widehat{\text{SLDR}}(\theta_{\min})$  and  $\widehat{\text{SLDR}}(\theta_{\max})$  on the spheroidal scattering model at (a)  $\theta_{\min} = 90^\circ$  and (b)  $\theta_{\max} = 150^\circ$  elevation angle. The red and blue curves in (a), (b), and (c) depict the isolines as (a)  $\text{SLDR}(\theta_{\min}) = \widehat{\text{SLDR}}(\theta_{\min})$  and (b)  $\text{SLDR}(\theta_{\max}) = \widehat{\text{SLDR}}(\theta_{\max})$  at 90 and 150° elevation, respectively. In (c) the intersections of the  $\widehat{\text{SLDR}}(\theta_{\min})$  and  $\widehat{\text{SLDR}}(\theta_{\max})$  isolines are shown. As input, hypothetical values of typical oblate particles with  $\text{SLDR}(\theta_{\min}) = -32$  dB and  $\text{SLDR}(\theta_{\max}) = -11$  dB were selected.

$\theta_{\max}$ . According to Reinking et al. (2002) and Matrosov et al. (2012), the relationship found is representative for oblate particles such as plate-like crystals, as depicted in Table 2. Regarding Fig. 6c presented in Sect. 3.2, we observe two intersections on both sides of  $\xi = 1$  and the choice of one of them requires an evaluation of the linear regression of SLDR from  $\theta_{\min}$  to  $\theta_{\max}$ . The associated distribution of SLDR presented in Fig. 5 confirms the assignment of ice particles to the oblate primary particle shape class due to the increase of SLDR from  $\theta_{\min}$  to  $\theta_{\max}$  and the exceeding of  $\text{lim}_{\text{SLDR}}$ . A value of  $\xi = 0.45$  is finally derived for this layer. The last step, according to the flow chart depicted in Fig. 4, is to apply the classification to the previously calculated profile of  $\xi$  (see Sect. 3.2) and to store the selected values. This distribution of particle shape delivers information about the vertical profile of ice particle shapes in a cloud which is a relevant indicator for understanding in-cloud processes, illustrated in Sect. 4.4. The next section aims to evaluate and validate the VDPS method by means of three case studies, representing the three previously described particle shape classes prolate, oblate, and isometric, and to demonstrate the ability of the VDPS method to detect microphysical processes.

## 4 Results

In this section, we demonstrate the capabilities of the VDPS retrieval by means of three case studies associated with the three main particle shape classes: isometric (rain, Sect. 4.1), prolate (columnar ice crystals, Sect. 4.2), and oblate (plate-like ice crystals, Sect. 4.3). A fourth case study is presented in Sect. 4.4 to conclude and open the discussion concerning the ability of VDPS to describe microphysical processes by a change in particle shape from the cloud top to the

cloud base. The four case studies were selected from the Cy-CARE observations, presented in Sect. 2. Temperature provides an important constraint for the particle shape, since laboratory studies show a clear relationship between particle shape, temperature, and supersaturation with respect to ice (Bailey and Hallett, 2009; Myagkov et al., 2016b). Given conditions of liquid water saturation, near  $T = -2^\circ\text{C}$ , the growth is plate-like, near  $T = -5^\circ\text{C}$  the growth is columnar, near  $T = -15^\circ\text{C}$  the growth again becomes plate-like, and at lower temperature, the growth becomes a mixture of thick plates and columns. A general meteorological situation is presented for each case study using the Cloudnet classification of targets based on MIRA-35 at zenith-pointing and auxiliary instrumentation (Illingworth et al., 2007) and an RHI scan of SLDR from  $\theta_{\min}$  to  $\theta_{\max}$ . Subsequently, the polarimetric parameter SLDR measured at  $\theta_{\min}$  and  $\theta_{\max}$  is combined with the spheroidal scattering model introduced in Sect. 3.2. We focus only on the selected layer to illustrate the case studies even though all layers are processed to obtain the vertical distribution of particle shape. The last step aims to deliver insights into the quantification of the primary particle shape classes, as explained in Sect. 3.3, with the vertical distribution of  $\xi$  in the investigated cloud. Since the proposed method uses the spheroidal approximation of pure-ice particles and assumes Rayleigh scattering, the derived values of  $\xi$  should be analyzed with care when the method is applied to rain and close to the melting layer. Since rain droplets corresponding to the maximum spectral line are often near spherical,  $\xi$  is valid since for spherical particles it is not sensitive to the refractive index. By contrast,  $\xi$  in the melting layer is likely not valid, because the depolarization observed in the melting layer is not caused by columnar shapes of particles but by their strongly irregular shapes, water coating

**Table 2.** Assignment of the characteristic values of SLDR at  $\theta_{\min} = 90^\circ$  and  $\theta_{\max} = 150^\circ$  elevation angle and their linear regressions as a function of  $\theta$ . The associated typical ranges of  $\xi$  are also given. Please note, values of  $\text{SLDR}(\theta_{\min})$  and  $\text{SLDR}(\theta_{\max})$  for the isometric shape class correspond to the detection limit of SLDR (see Sect. 2.1). The limit values are  $\text{lim}_{\text{SLDR}} = 0.1 \text{ dB deg}^{-1}$  and  $\text{lim}_{\text{pro}} = -25 \text{ dB}$ .

Shape class	Linear regression	Value at $90^\circ$	Value at $150^\circ$	Polarizability ratio $\xi$
Oblate	$\frac{\partial \text{SLDR}}{\partial \theta} > \text{lim}_{\text{SLDR}}$	$\text{SLDR}(\theta_{\min}) = -30 \text{ dB}$	$\text{SLDR}(\theta_{\max}) = -10 \text{ dB}$	$\xi = 0.2\text{--}0.8$
Isometric	$\frac{\partial \text{SLDR}}{\partial \theta} < \text{lim}_{\text{SLDR}}$	$\text{SLDR}(\theta_{\max}) = -35 \text{ dB}$	$\text{SLDR}(\theta_{\min}) = -35 \text{ dB}$	$\xi = 0.8\text{--}1.2$
Prolate	$\frac{\partial \text{SLDR}}{\partial \theta} < \text{lim}_{\text{SLDR}}$	$\text{SLDR}(\theta_{\min}) = -20 \text{ dB}$	$\text{SLDR}(\theta_{\max}) = -20 \text{ dB}$	$\xi = 1.2\text{--}2.4$

(and associated fluctuations of apparent density), and their large size. This section aims to demonstrate that the VDPS method gives concordant results with the observations for the three primary particle shape classes, isometric, prolate, and oblate particles, introduced in Sect. 3.2, and that it is a promising supplemental technique for studying cloud microphysical processes.

**4.1 Isometric particle shape class: rain event on 13 February 2017 at 13:31 UTC**

The first case study concentrates on the occurrence of rain, i.e., hydrometeors representative for the primary isometric particle shape class. Measurements were recorded on 13 February 2017 during an RHI scan from 13:31 to 13:33 UTC in Limassol. The studied cloud system, enframed by the black box in the Cloudnet target classification mask shown in Fig. 7, was identified to contain rain droplets at heights between 300 and 1300 m. The sudden drop of the melting layer height from 1300 m to around 1000 m height that is visible right at the time of the RHI scan is an artifact of the melting layer detection scheme of Cloudnet, which switched from a fall-velocity-based detection to the  $0^\circ\text{C}$ -dewpoint level as threshold for the melting layer identification. However, the actual melting layer is well recognizable in Fig. 8 by means of the observed high values of SLDR at around 1300 m height. The Cloudnet classification indicates a mixed-phase layer at 1800 m height. For this case study, we are particularly interested in the rain from 300 to 1200 m height.

Figure 8 shows the RHI scan of SLDR from  $90$  to  $150^\circ$  elevation angle which was performed at 13:31 UTC. Values of SLDR from  $\theta_{\min}$  to  $\theta_{\max}$  are low (around  $-30 \text{ dB}$ ) and constant at heights below the melting layer, which is in agreement with what can be expected from scattering by isometric particles, as explained in Sect. 3.3. To illustrate this case study, we will focus only on one layer located at the height level from 868 to 899 m, represented by the black line on the y axis in Fig. 8. In Fig. 9b, the intersection of  $\widehat{\text{SLDR}}(\theta_{\min})$  and  $\widehat{\text{SLDR}}(\theta_{\max})$  is detectable by the red and blue curves which match the data of SLDR at  $\theta_{\min}$  and  $\theta_{\max}$ , respectively, with the simulated data  $\widehat{\text{SLDR}}$  from the spheroidal scattering model. We can distinctly notice the presence of two intersections between  $\widehat{\text{SLDR}}(\theta_{\min})$  and  $\widehat{\text{SLDR}}(\theta_{\max})$  from either

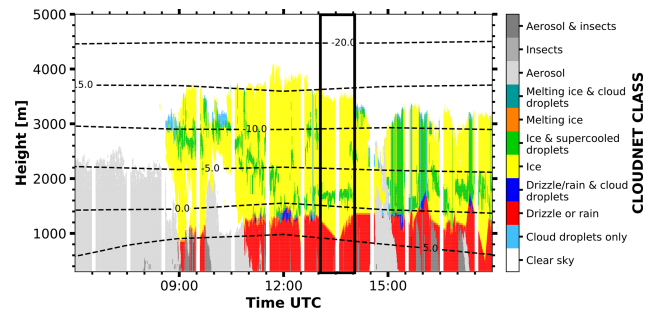


**Figure 7.** Cloudnet target classification mask as derived from observations in Limassol on 13 February 2017 from 06:00 to 18:00 UTC. The black box denotes the RHI scan that is discussed in further detail in Sect. 4.1.

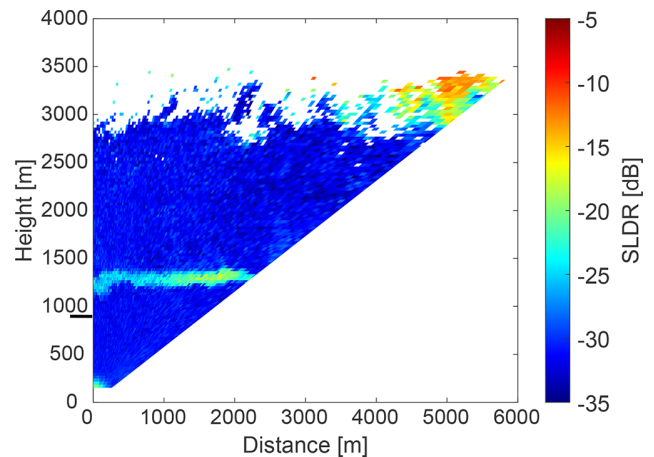


**Figure 8.** RHI scan of SLDR observed on 13 February 2017, at 13:31 UTC in Limassol from  $90$  to  $150^\circ$  elevation angle. The horizontal black line on the y axis marks the height of the layer analyzed in Fig. 9.

side of the dashed red line, resulting in  $\xi = 0.9$  and  $\xi = 1.1$ . In Fig. 9a, the slope of the linear regression  $\frac{\partial \text{SLDR}}{\partial \theta}$  is constant between  $\theta_{\min}$  and  $\theta_{\max}$  where  $\text{SLDR}(\theta_{\min}) < \text{lim}_{\text{pro}}$  and  $\text{SLDR}(\theta_{\max}) < \text{lim}_{\text{pro}}$  and  $\frac{\partial \text{SLDR}}{\partial \theta} < \text{lim}_{\text{SLDR}}$ . Regarding Table 2, this configuration describes the isometric primary particle shape class. Finally, the vertical distribution of  $\xi$  in the cloud is calculated following Sect. 3.3 and shown in Fig. 10. Concerning the observations, the melting layer is well iden-

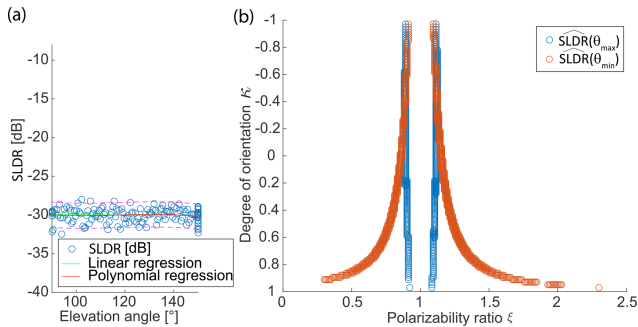


**Figure 9.** Detailed view of the isometric-shape case study presented in Fig. 8 for the layer from 868 to 899 m height. **(a)** Distribution of measured values of SLDR from  $\theta_{\min}$  to  $\theta_{\max}$  elevation angle and associated linear and polynomial fits. The dashed pink lines in **(a)** correspond to the 95 % prediction interval from the third-degree polynomial function, used to determine the intersection of  $\overline{\text{SLDR}}(\theta_{\min})$  and  $\overline{\text{SLDR}}(\theta_{\max})$ . **(b)** Intersection between  $\overline{\text{SLDR}}(\theta_{\min})$  and  $\overline{\text{SLDR}}(\theta_{\max})$  at  $\theta_{\min}$  and  $\theta_{\max}$ , respectively.

tified by a variable  $\xi$ , as explained in the introduction of Sect. 4, in the height range from 1250 to 1350 m. Below this layer,  $\xi$  takes values around 1, which describes isometric or less dense particles (Sect. 3.2). Looking at the Cloudnet classification (Fig. 7), the drizzle-or-rain class dominates the measurement at heights below approximately 1000 m height, which can be extended to the melting layer at around 1300 m height, taking into account the misidentified drop due to the melting layer detection of Cloudnet, as previously explained. Figure 7 shows, in the black box, a temperature higher than  $0^{\circ}\text{C}$  in this layer, which confirms the presence of liquid droplets, i.e., isometric particles. Application of the VDPS approach results in derivation of the same isometric primary particle shape class as determined based on the auxiliary observations (temperature and Cloudnet classification). With respect to the presented case it is noteworthy that it is likely that the observed rain droplets were small in size. This is corroborated by the absence of any elevation dependency of SLDR (Fig. 9). In the case of strong rain, the oblateness of droplets would become apparent as SLDR increases from zenith pointing to  $150^{\circ}$  elevation angle, as we observed in some situations of convective rain in Limassol during the CyCARE campaign (Sect. 2.2). Above the melting layer from 1700 to 2800 m height, the VDPS method derived isometric or less dense particles, as well. Given that temperatures are below freezing level at these heights and that Cloudnet identified a mix of ice and supercooled droplets, it is likely that these isometric or less dense particles are the result of mixed-phase cloud processes, such as riming or aggregation, which cannot unambiguously be identified solely with the VDPS method. Based on the VDPS method, the height level of the particle shape transition can be determined to be present at around 2800 m. Above,  $\xi$  was found to be well below 1, representing oblate particles, whose formation is also corrobo-

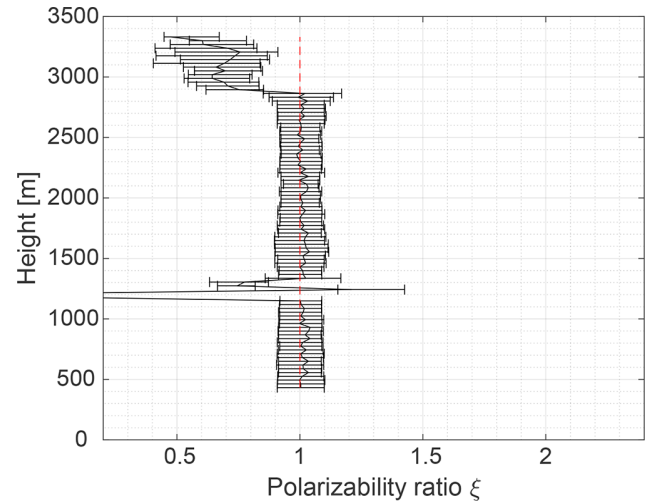


**Figure 10.** Vertical distribution of  $\xi$  as calculated with the VDPS method for each layer of the isometric-shape case study observed in Limassol on 13 February 2017, 13:31 UTC.

rated by the ambient temperatures of around  $-15^{\circ}\text{C}$  at this height level (see Fig. 7). Applicability of the VDPS method is in the present case limited with respect to the interpretation of the microphysical process which led to the formation of the layer with isometric particle shape between approximately 1500 and 2700 m height. Doppler spectral methods or multi-frequency approaches could help here to investigate the possible contributions of riming and aggregation (Kneifel et al., 2016; Radenz et al., 2019; Kalesse-Los et al., 2022; Vogl et al., 2022).

#### 4.2 Prolate particle shape class: columnar crystals on 4 January 2017 at 04:30 UTC

The second case study chosen to evaluate the VDPS method is dedicated to the characterization of columnar crystals. The corresponding measurement was recorded in Limassol on 8 December 2016 during an RHI scan from 00:31 to 00:33 UTC. Figure 11 presents the Cloudnet classification for the time range from 00:00 to 03:00 UTC on 8 December 2016, with the selected case study marked by the black frame. Figure 12 shows the RHI scans of SLDR from  $90^{\circ}$  to  $150^{\circ}$  elevation angle at 00:31 UTC.

In this RHI scan, high values of SLDR are observed at all elevation angles (between  $-20$  and  $-15$  dB), suggesting that the cloud is very homogeneous and that ice particles have a high capability to depolarize the returned radar signals. According to Reinking et al. (2002), particles having a SLDR from  $-20$  to  $-15$  dB can be classified at first glance as needles or hollow columns. This constellation excludes isometric particles and oblate particles and is a specific property of columnar crystals (see Table 2). As for the first case study, the retrieval is visualized only for one specific layer, which in this case spans from 2458 to 2490 m height, indicated by

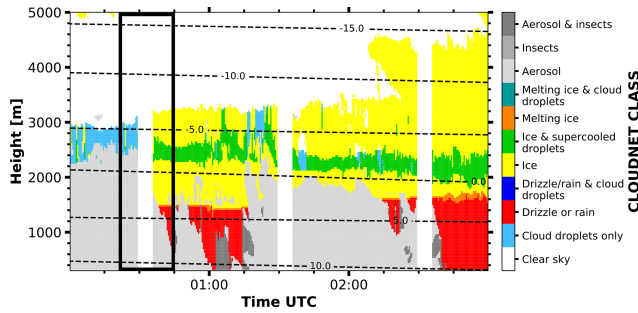


**Figure 11.** Cloudnet target classification mask as derived for observations in Limassol on 8 December 2016 from 00:00 to 03:00 UTC. The black box denotes the RHI scan that is discussed in further detail in Sect. 4.2.

the black line on the y axis in Fig. 12. Figure 13a shows the SLDR linear regression represented by the green line, which confirms that  $\frac{\partial \text{SLDR}}{\partial \theta} < \text{lim}_{\text{SLDR}}$ . The polynomial fit represented by the red curve is used at  $\theta_{\min}$  to  $\theta_{\max}$  to calculate  $\text{SLDR}(\theta_{\min})$  and  $\text{SLDR}(\theta_{\max})$ , as elaborated in Section 3.2. In Fig. 13b, once again two intersections of  $\text{SLDR}(\theta_{\min})$  and  $\text{SLDR}(\theta_{\max})$  exist for this layer. Considering the constant distribution ( $\frac{\partial \text{SLDR}}{\partial \theta} < \text{lim}_{\text{SLDR}}$ ) and high values of SLDR ( $\text{SLDR}(\theta_{\min}) > \text{lim}_{\text{pro}}$  and  $\text{SLDR}(\theta_{\max}) > \text{lim}_{\text{pro}}$ ), we can identify the intersection in the columnar particle shape class (see Table 2), resulting in  $\xi > 1$  and  $\kappa < -0.8$  as the most likely one. Figure 14 shows the vertical profile of  $\xi$ , which confirms the dominance of prolate particles in the investigated cloud. Accordingly, the Cloudnet classification, shown in Fig. 11 (black box), classifies the hydrometeors before the RHI scan as supercooled liquid droplets, and after the RHI scan as ice-containing and partly mixed-phase layer down to about 1500 m height. A rain event occurs a few minutes after the RHI scan, defining drizzle or rain. The temperature of the investigated case ranges from  $-3^\circ\text{C}$  at the cloud base and  $-7^\circ\text{C}$  at the cloud top. This temperature range is characteristic for the formation of hydrometeors in the columnar particle shape class, which demonstrates the ability of VDPS to derive prolate particles.

#### 4.3 Oblate particle shape class: plate-like crystals on 4 January 2017 at 01:30 UTC

The third case study aims to describe oblate particles, such as plate-like crystals. The corresponding measurement was recorded in Limassol on 4 January 2017 during an RHI scan from 01:31 to 01:33 UTC. The observed cloud system is marked by the black frame in Fig. 15. The observation was characterized by the presence of a relatively homogeneous liquid-topped ice cloud in the height range from 3200 to 4200 m. Figure 16 shows the RHI scan of SLDR from  $90$  to  $150^\circ$  elevation angle at 01:31 UTC. An increase of SLDR from  $-30$  to  $-10$  dB between  $\theta_{\min}$  and  $\theta_{\max}$  is visible. The linear regression is represented by the green line in Fig. 17a,

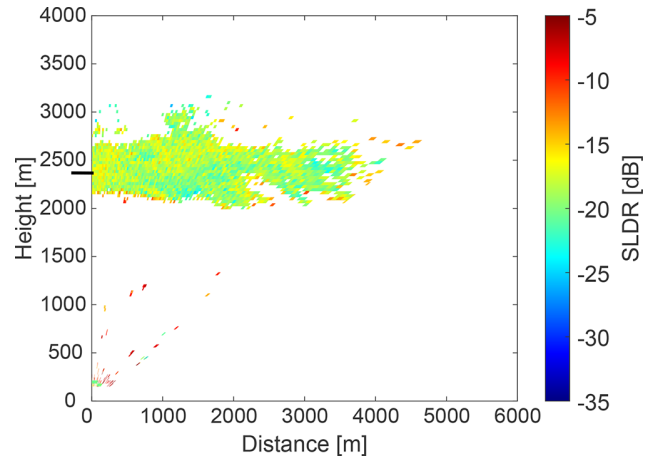


**Figure 12.** RHI scan of SLDR on 8 December 2016, at 00:31 UTC, Limassol, from  $90$  to  $150^\circ$  elevation angle. The horizontal black line on the y axis marks the height of the layer analyzed in Fig. 13.

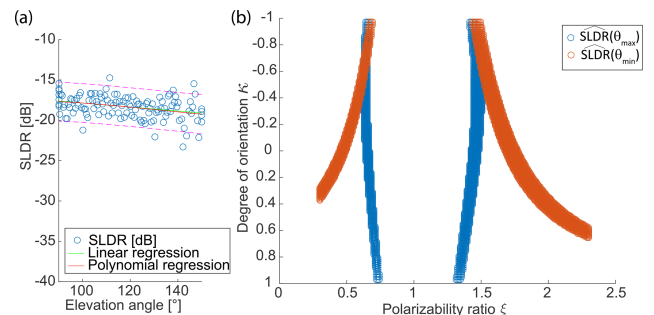


**Figure 13.** Detailed view of the columnar-shape case study presented in Fig. 12 for the layer from 2458 to 2490 m height. **(a)** Distribution of measured values of SLDR from  $\theta_{\min}$  to  $\theta_{\max}$  elevation angle and associated linear and polynomial fits. The dashed pink line in **(a)** corresponds to the 95 % prediction interval from the third-degree polynomial function, used to determine the intersection of  $\text{SLDR}(\theta_{\min})$  and  $\text{SLDR}(\theta_{\max})$ . **(b)** Intersection between  $\text{SLDR}(\theta_{\min})$  and  $\text{SLDR}(\theta_{\max})$  at  $\theta_{\min}$  and  $\theta_{\max}$ , respectively.

which exemplarily shows the retrieval for the layer from 3300 to 3331 m height, represented by the black line on the y axis in Fig. 16. In this case,  $\frac{\partial \text{SLDR}}{\partial \theta} > \text{lim}_{\text{SLDR}}$ .  $\text{SLDR}(\theta_{\min})$  and  $\text{SLDR}(\theta_{\max})$  are calculated based on the values retrieved from the polynomial fit at  $\theta_{\min}$  and  $\theta_{\max}$ , i.e., the red curve represented in Fig. 17a. In Fig. 17b, we see two intersections between the isolines of  $\text{SLDR}(\theta_{\min})$  and  $\text{SLDR}(\theta_{\max})$ . This configuration, associated with a positive linear regression of the polarimetric parameter SLDR (see Table 2), implies selecting the intersection at  $\xi < 1$  and  $\kappa > 0.8$  for determination of the exact polarizability ratio, which corresponds to the oblate primary particle shape class. The vertical distribution of  $\xi$  presented in Fig. 18 indicates  $\xi < 1$  for all layers in the investigated cloud. The values of  $\xi$  are relatively constant around 0.4 from 3100 to 3600 m height corresponding



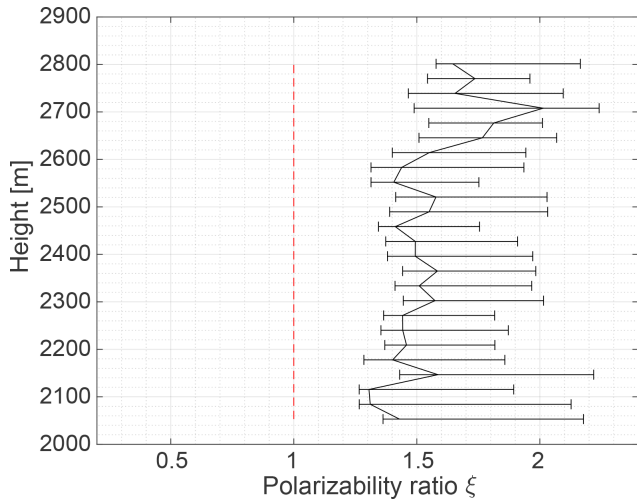


**Figure 14.** Polarizability ratio  $\xi$  calculated for each layer with the VDPS method for the columnar-shape case study, observed in Limassol on 8 December 2016, at 00:31 UTC.

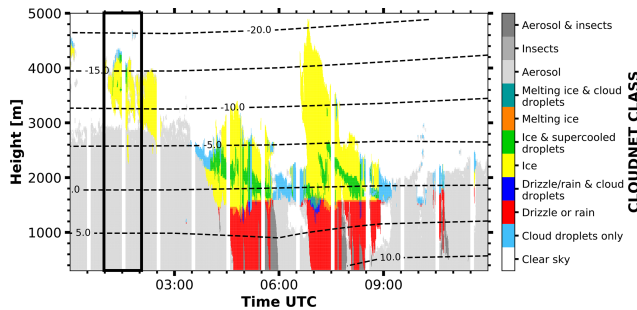


**Figure 15.** Cloudnet target classification mask as derived for observations in Limassol on 4 January 2017 from 00:00 to 12:00 UTC. The black box denotes the RHI scan that is discussed in further detail in Sect. 4.3.

to particles which are strongly oblate and rather dense, most likely pointing to the class of thick plate crystals (Reinking et al., 2002; Matrosov et al., 2012). On the other hand, above 3600 m height,  $\xi \approx 0.55$  was observed, representing particles which are likely less dense such as plates or dendritic crystals. In the Cloudnet classification shown in Fig. 15, where the period of approximately 1 h around the investigated RHI scan is indicated by the black rectangle, ice crystals and contributions of supercooled liquid droplets at the cloud top were identified. The temperature in the cloud ranges from  $-15\text{ }^{\circ}\text{C}$  at the cloud top to  $-10\text{ }^{\circ}\text{C}$  at the cloud base. Laboratory studies suggest that, in this temperature range, the primary formation of plate-like ice crystals is most likely to occur (Bailey and Hallett, 2009). Hence, there is a remarkably good agreement between results of the VDPS method and observations for this case study as well.

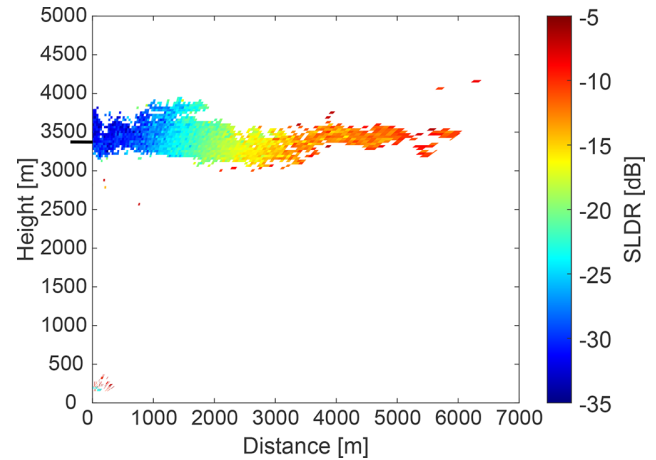


**Figure 16.** RHI-scan of SLDR on 4 January 2017, at 01:31 UTC in Limassol from  $90$  to  $150^{\circ}$  elevation angle. The horizontal black line on the y axis marks the height of the layer analyzed in Fig. 17.

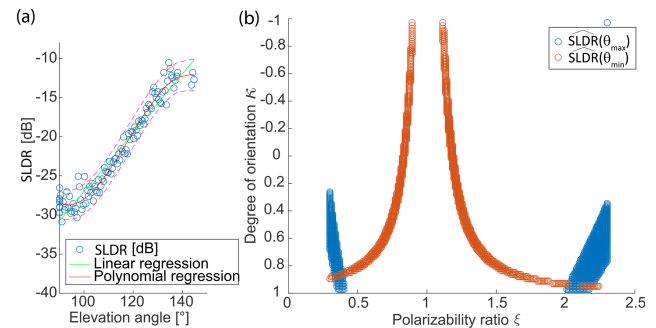


**Figure 17.** Detailed view into the plate-like-shape case study presented in Fig. 8 for the layer from 3300 to 3331 m height. **(a)** Distribution of measured values of SLDR from  $\theta_{\min}$  to  $\theta_{\max}$  elevation angle and associated linear and polynomial fits. The dashed pink line in **(a)** corresponds to the 95% prediction interval from the third-degree polynomial function, used to determine the intersection of  $\overline{\text{SLDR}}(\theta_{\min})$  and  $\overline{\text{SLDR}}(\theta_{\max})$ . **(b)** Intersection between  $\overline{\text{SLDR}}(\theta_{\min})$  and  $\overline{\text{SLDR}}(\theta_{\max})$  at  $\theta_{\min}$  and  $\theta_{\max}$ , respectively.

#### 4.4 Microphysical transformation: case study from 2 February 2017, 13:31 UTC

By means of a final case study, the potential of the VDPS method for exploration of the vertical evolution of particle shapes from the cloud top to the cloud base is discussed. The corresponding measurement was recorded in Limassol on 2 January 2017. In Fig. 19, the Cloudnet target classification mask of the observed cloud system is shown. The black frame in Fig. 19 highlights the time period around the RHI scan at 13:31 (vertical white bar), which will be analyzed here. As can be seen from the Cloudnet classification, ice crystals were identified at all heights from the cloud top (around 8500 m) down to the melting layer, which was classified at a height of around 1700 m. Only at heights between



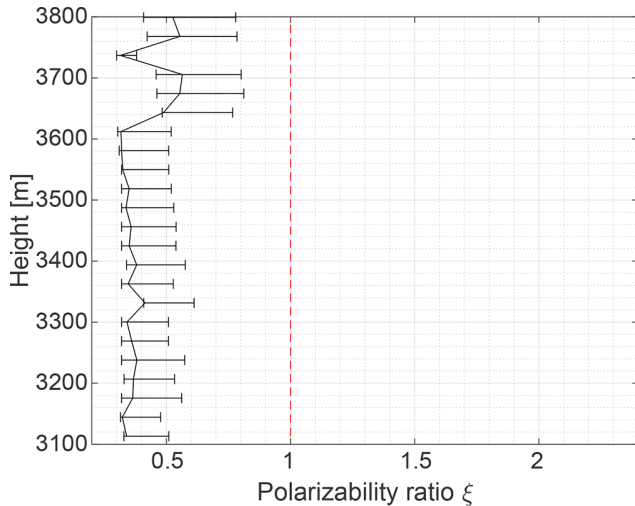


**Figure 18.** Polarizability ratio  $\xi$  calculated for each layer with the VDPS method for a plate-like-shape case study observed in Limassol on 4 January 2017 at 01:31 UTC.

around 2000 and 2500 m were few data points of mixed-phase conditions identified. Also in Fig. 20, which shows the 13:31 UTC RHI scan of SLDR from 90 to 150° elevation angle, the melting layer is well represented at around 1700 m height by increased values of SLDR at all elevation angles. Focusing on the height range above the melting layer, the elevation dependency of SLDR shows a distinct evolution from the cloud top to the bottom. At the top of the cloud, at around 8000 m height, we can observe a strong increase of SLDR from  $\theta_{\min}$  to  $\theta_{\max}$  (−30 dB at  $\theta_{\min}$  and −5 dB at  $\theta_{\max}$ ). Moving away from the cloud top toward the melting layer, the increase in SLDR from  $\theta_{\min}$  to  $\theta_{\max}$  becomes gradually less pronounced. Slightly above the melting layer ( $\approx 2000$  m height), SLDR assumes values of around −30 dB at all elevation angles. The gradual change of the elevation dependency of SLDR from the cloud top to the cloud base translates into the vertical distribution of the polarizability ratio, as is illustrated in Fig. 21. From 8000 to 2000 m height, the polarizability ratio  $\xi$  increases gradually from 0.3, corresponding to very oblate and dense particles, such as plates, to 0.8 corresponding to less dense oblate particles, such as dendrites or aggregates. Between 2000 m height and the melting layer, located at 1700 m height, the polarizability ratio  $\xi$  is close to 1 corresponding to particles with low density or generally spherical particles. This gradual increase in  $\xi$  informs of a vertical change in particle shape while the ice crystals sedimented through the cloud system. As outlined earlier, a direct determination of the types of microphysical processes that occurred in this case cannot be achieved, as further constraints must be incorporated for a thorough interpretation as is outlined in Sect. 5.

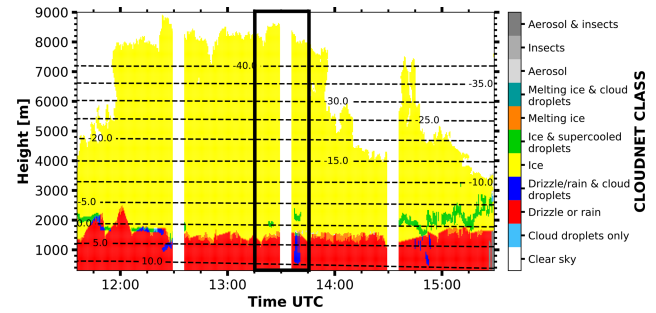


**Figure 19.** Cloudnet target classification mask as derived for observations in Limassol on 12 February 2017 from 11:30 to 15:30 UTC.

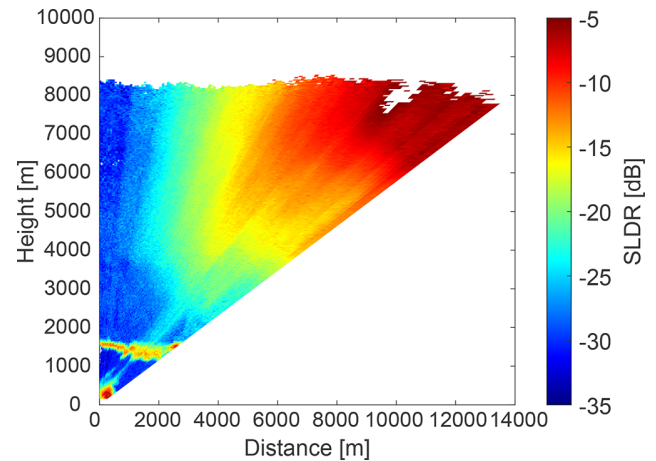


**Figure 20.** RHI scan of SLDR from 90 to 150° elevation angle observed in Limassol on 2 January 2017 at 13:31 UTC.

## 5 Discussion and conclusions

In this article, the vertical distribution of particle shape (VDPS) method was introduced. Based on earlier studies, which have succeeded in demonstrating the applicability of polarimetric parameters from cloud radar to estimate the particle shape (Matrosov et al., 2012; Myagkov et al., 2016a), this new approach aids one in characterizing the shape of cloud particles from scanning SLDR-mode cloud radar observations. The new VDPS method is based only on a single polarimetric parameter – SLDR. Another novelty of the VDPS method is the idea that a profile of the polarizability ratio can be used not only to derive the shape of pristine ice crystals at cloud tops (as done in Myagkov et al., 2016a, b) but also as an indicator of microphysical processes affecting particle shape and/or apparent density in deep precipitating clouds. In addition, the VDPS method is more versatile than the original approach of Myagkov et al. (2016a), which was developed for hybrid-mode cloud radars, requiring a complex calibration of ZDR and correlation coefficient. We will compare the two methods in an upcoming campaign in Switzerland (winter 2023/2024), where an SLDR (Metek

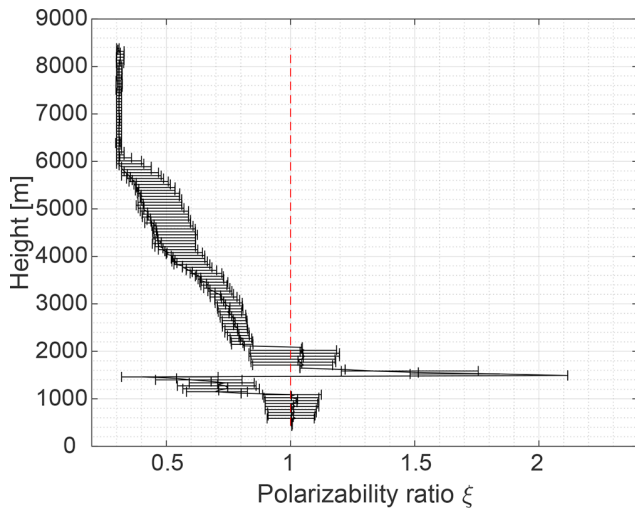


**Figure 21.** Profile of the polarizability ratio  $\xi$  on 2 January 2017 at 13:31 UTC in Limassol, as obtained from the RHI scan of SLDR presented in Fig. 20.

S/N MBR5) and a hybrid-mode radar (Metek S/N MBR7) will operate co-located next to each other.

The 45°-slanted linear depolarization (SLDR) mode was specifically chosen for the purpose of minimizing the influence of fluctuations in the particle orientation during sedimentation, called “the wobbling effect” (Matrosov et al., 2001), while providing well suited and relatively easy observable input parameters for the shape retrieval. The VDPS approach represents a new, versatile way to study microphysical processes by combining a spheroidal scattering model (Myagkov et al., 2016b) applied only to SLDR. In this paper, the VDPS method was introduced and validated by means of case studies collected in the frame of the CyCARE field campaign (Limassol, Cyprus), for three representative shape classes – oblate, isometric, and prolate particles – which are characterized by polarizability ratios of  $\xi < 1$ ,  $\xi \approx 1$ , and  $\xi > 1$ , respectively. A fourth case study demonstrated the potential of the VDPS method for tracking of the evolution of the ice crystal shape between the top and base of a deep cloud system. Before application of the VDPS method to the case studies, the algorithm was tested and calibrated with success based on observational datasets from two field campaigns, CyCARE in Limassol, Cyprus, and DACAPO-PESO in Punta Arenas, Chile (Radenz et al., 2021), which sums up to 3 years of SLDR measurements at two different places. It is important to highlight that we could not validate the method using in situ observations throughout the two campaigns. It is nevertheless the goal of the authors of this study to aim at deployments of the SLDR-mode scanning cloud radar in campaigns where in situ observations are available.

The vertical distribution of the polarizability ratio  $\xi$  is valuable because it informs about the transformation of apparent particle shape or density in an investigated cloud from

top to bottom, which shows that microphysical processes are occurring. Based on the information about the vertical distribution of particle shape in a cloud, the VDPS method provides valuable constraints for microphysical fingerprinting studies (Sect. 4.4). The height-resolved view of the vertical distribution and evolution of particle shape in a cloud is helpful for studying and characterizing mixed-phase cloud processes in the onset phase of precipitation. While isometric, columnar, and oblate particle shapes can well be distinguished with the VDPS method, discrimination between graupel (formed by riming) and aggregates (formed by aggregation) remains a challenge and is currently not possible solely with the VDPS method. Nevertheless, both processes can potentially be inferred based on the vertical evolution of  $\xi$  between cloud top and cloud base. In the future, we therefore plan to associate the VDPS method with Doppler spectral methods in order to detect supercooled liquid droplets in mixed-phase clouds and to estimate the fall velocity of particles, which provide relevant constraints for the discrimination between riming and aggregation processes. Indeed, riming processes require the presence of supercooled liquid droplets and the graupel particles fall faster than aggregates because of their higher density (Kneifel et al., 2016; Vogl et al., 2022).

Besides the aforementioned strengths of the VDPS method, there are also certain limitations, which can eventually be overcome in future development steps. The first one corresponds to the radar antenna quality, as it determines the calibration of SLDR. The polarimetric parameter SLDR is intrinsically dependent on the calibration of the antenna and the differential phase of the transceiver unit. Care must be taken to ensure a good calibration of the radar system. A good co-cross-channel isolation should be aspired to in order to obtain the highest accuracy of the retrieval, especially for values of  $\xi$  that are close to 1. In addition, turbulence, horizontal wind, and radar beam width, especially at large off-zenith-pointing angles, can lead to a broadening of the Doppler spectra, which has the potential to impact the spectral peak values in both channels (Kollias et al., 2011). Spectral broadening becomes noteworthy when particles with distinct polarimetric signatures are blended into a single spectral line, and it becomes particularly relevant when substantial turbulence is present (typically on the order of several meters per second). However, the spectral broadening would not considerably change observed polarimetric signatures in the case of pristine ice crystals at the cloud top, or when only one type of hydrometeor is present in a cloud volume. Finally, in our study we assume Rayleigh scattering and describe particle shapes according to the aspect ratio and the permittivity. In reality, ice crystal shapes are more complex and need a more sophisticated scattering method to accurately capture scattering of particles with axis lengths exceeding the range of the Rayleigh scattering regime. This holds definitely true for absolute quantities such as reflectivity at wavelengths shorter than C-band (Lu et al., 2016).

However, a recent study by Matrosov (2021) demonstrates that the influence of non-Rayleigh scattering is weak for polarimetric variables such as LDR. As a likely reason for this behavior, Matrosov (2021) hypothesizes that polarimetric variables are differential (rather than absolute) quantities representing differences/ratios of radar parameters at two orthogonal polarizations. T-Matrix or DDA methods provide many more degrees of freedom concerning the microphysics of the scattering hydrometeors. If these are applied to realistic hydrometeor populations, a model-based validation of the hypothesis of Matrosov (2021) will be feasible.

In its current development state, the VDPS method is also only capable of investigating the shape of the hydrometeor population that determines the main peak of the co-channel Doppler spectrum, as characterized by the highest peak of each Doppler spectrum obtained during an RHI scan at any given height level. However, a new approach taking into account the comparison between main peaks detected in the co- and cross-channels can give more information about the ice crystal populations in a volume: if the main peaks are similar in the co- and cross-channels, it means that the main hydrometeor population depolarizes the most. On the other hand, the presence of different main peaks in the co- and cross-polarized Doppler spectra would imply the presence of a second hydrometeor population which depolarizes strongly, while still a non-polarizing hydrometeor population dominates the co-channel signal.

The technique can currently thus not be used for evaluating the RHI scans for coexistence of several particle populations, as they might be superimposed by means of their differential fall velocities collected in a Doppler spectrum. Such peak separation techniques have already been developed for vertically pointing cloud radar measurements (Kalesse et al., 2019; Radenz et al., 2019) and can potentially be adapted for scanning cloud radars in the near future.

Overall, the VDPS technique has the potential to become a standard procedure in the analysis of long-term observations from scanning SLDR cloud radar systems. Given the broad availability of scanning LDR-mode cloud radars in Europe, the VDPS method provides good reasoning to update these to SLDR mode with low effort and investment.

*Code and data availability.* The cloud radar raw data and retrieval codes are available upon request. Please contact the first or second author. Cloudnet data are available at <https://hdl.handle.net/21.12132/2.a056a828a6b94d1f> (Mamouri, 2021). For plotting of the measurement data the tool pyLARDA (Bühl et al., 2021) was used.

*Author contributions.* AT developed the VDPS method, analyzed the data, and drafted the manuscript supervised by PS. JB conducted the CyCARE campaign and operated LACROS. PS, MR, and JB generated the Cloudnet datasets and supervised the data processing

chain. AM supported the starting phase of the development work on the VDPS method and developed the spheroidal scattering model.

*Competing interests.* The contact author has declared that neither they nor their co-authors have any competing interests.

*Disclaimer.* Publisher's note: Copernicus Publications remains neutral with regard to jurisdictional claims made in the text, published maps, institutional affiliations, or any other geographical representation in this paper. While Copernicus Publications makes every effort to include appropriate place names, the final responsibility lies with the authors.

*Special issue statement.* This article is part of the special issue "Fusion of radar polarimetry and numerical atmospheric modelling towards an improved understanding of cloud and precipitation processes (ACP/AMT/GMD inter-journal SI)". It is not associated with a conference.

*Acknowledgements.* Development of the VDPS method was funded by the Deutsche Forschungsgemeinschaft (DFG – German Research Foundation) project PICNICC (SE2464/1-1 and KA4162/2-1). The authors wish to thank Cyprus University of Technology, Limassol, Cyprus, for their logistic and infrastructural support during the LACROS deployment. We gratefully acknowledge the ACTRIS Cloud Remote Sensing Unit for making the Cloudnet datasets publicly available. LACROS operations were supported by the European Union (EU) Horizon 2020 (ACTRIS; grant no. 654109) and the Seventh Framework Programme (BACCHUS; grant no. 603445). The authors also wish to thank Metek GmbH, Elmshorn, for the technical support related to the MIRA-35 radar.

*Financial support.* This work was funded by the Deutsche Forschungsgemeinschaft (DFG – German Research Foundation) project PICNICC (grant nos. SE2464/1-1 and KA4162/2-1) and the European Union (EU) Horizon 2020 project (ACTRIS; grant no. 654109).

The publication of this article was funded by the Open Access Fund of the Leibniz Association.

*Review statement.* This paper was edited by Raquel Evaristo and reviewed by two anonymous referees.

## References

Ansmann, A., Mamouri, R.-E., Hofer, J., Baars, H., Althausen, D., and Abdullaev, S. F.: Dust mass, cloud condensation nuclei, and ice-nucleating particle profiling with polarization lidar: updated POLIPHON conversion factors from global

- AERONET analysis, *Atmos. Meas. Tech.*, 12, 4849–4865, <https://doi.org/10.5194/amt-12-4849-2019>, 2019.
- Avramov, A. and Harrington, J. Y.: Influence of parameterized ice habit on simulated mixed phase Arctic clouds, *J. Geophys. Res.-Atmos.*, 115, D03205, <https://doi.org/10.1029/2009JD012108>, 2010.
- Bailey, M. P. and Hallett, J.: A Comprehensive Habit Diagram for Atmospheric Ice Crystals: Confirmation from the Laboratory, AIRS II, and Other Field Studies, *J. Atmos. Sci.*, 66, 2888–2899, <https://doi.org/10.1175/2009JAS2883.1>, 2009.
- Brdar, S. and Seifert, A.: McSnow: A Monte-Carlo Particle Model for Riming and Aggregation of Ice Particles in a Multidimensional Microphysical Phase Space, *J. Adv. Model. Earth Syst.*, 10, 187–206, <https://doi.org/10.1002/2017MS001167>, 2018.
- Bringi, V. and Chandrasekar, V.: *Polarimetric Doppler Weather Radar: Principles and Applications*, ISBN 9780521623841, Revised ed. Edition (8. September 2005), <https://doi.org/10.1017/CBO9780511541094>, Cambridge University Press, 2001.
- Bühl, J., Seifert, P., Myagkov, A., and Ansmann, A.: Measuring ice- and liquid-water properties in mixed-phase cloud layers at the Leipzig Cloudnet station, *Atmos. Chem. Phys.*, 16, 10609–10620, <https://doi.org/10.5194/acp-16-10609-2016>, 2016.
- Bühl, J., Seifert, P., Radenz, M., Baars, H., and Ansmann, A.: Ice crystal number concentration from lidar, cloud radar and radar wind profiler measurements, *Atmos. Meas. Tech.*, 12, 6601–6617, <https://doi.org/10.5194/amt-12-6601-2019>, 2019.
- Bühl, J., Radenz, M., Schimmel, W., Vogl, T., Röttenbacher, J., and Lochmann, M.: pyLARDA v3.2 (v3.2), Zenodo [data set], <https://doi.org/10.5281/zenodo.4721311>, 2021.
- Draine, B. T. and Flatau, P. J.: Discrete-Dipole Approximation For Scattering Calculations, *J. Opt. Soc. Am. A*, 11, 1491–1499, <https://doi.org/10.1364/JOSAA.11.001491>, 1994.
- Fan, J., Han, B., Varble, A., Morrison, H., North, K., Kollias, P., Chen, B., Dong, X., Giangrande, S. E., Khain, A., Lin, Y., Mansell, E., Milbrandt, J. A., Stenz, R., Thompson, G., and Wang, Y.: Cloud-resolving model intercomparison of an MC3E squall line case, *J. Geophys. Res.-Atmos.*, 122, 9351–9378, <https://doi.org/10.1002/2017JD026622>, 2017.
- Fukuta, N. and Takahashi, T.: The Growth of Atmospheric Ice Crystals: A Summary of Findings in Vertical Supercooled Cloud Tunnel Studies, *J. Atmos. Sci.*, 56, 1963–1979, [https://doi.org/10.1175/1520-0469\(1999\)056<1963:TGOAIC>2.0.CO;2](https://doi.org/10.1175/1520-0469(1999)056<1963:TGOAIC>2.0.CO;2), 1999.
- Görsdorf, U., Lehmann, V., Bauer-Pfundstein, M., Peters, G., Vavriv, D., Vinogradov, V., and Volkov, V.: A 35-GHz Polarimetric Doppler Radar for Long-Term Observations of Cloud Parameters Description of System and Data Processing, *J. Atmos. Ocean. Technol.*, 32, 675–690, <https://doi.org/10.1175/JTECH-D-14-00066.1>, 2015.
- Illingworth, A. J., Hogan, R. J., O'Connor, E., Bouniol, D., Brooks, M. E., Delanoé, J., Donovan, D. P., Eastment, J. D., Gaussiat, N., Goddard, J. W. F., Haeffelin, M., Baltink, H. K., Krasnov, O. A., Pelon, J., Piriou, J.-M., Protat, A., Russchenberg, H. W. J., Seifert, A., Tompkins, A. M., van Zadelhoff, G.-J., Vinit, F., Willén, U., Wilson, D. R., and Wrench, C. L.: Cloudnet: Continuous Evaluation of Cloud Profiles in Seven Operational Models Using Ground-Based Observations, *B. Am. Meteorol. Soc.*, 88, 883–898, <https://doi.org/10.1175/BAMS-88-6-883>, 2007.
- Kalesse, H., Vogl, T., Paduraru, C., and Luke, E.: Development and validation of a supervised machine learning radar Doppler spectra peak-finding algorithm, *Atmos. Meas. Tech.*, 12, 4591–4617, <https://doi.org/10.5194/amt-12-4591-2019>, 2019.
- Kalesse-Los, H., Schimmel, W., Luke, E., and Seifert, P.: Evaluating cloud liquid detection against Cloudnet using cloud radar Doppler spectra in a pre-trained artificial neural network, *Atmos. Meas. Tech.*, 15, 279–295, <https://doi.org/10.5194/amt-15-279-2022>, 2022.
- Kneifel, S., Kollias, P., Battaglia, A., Leinonen, J., Maahn, M., Kalesse, H., and Tridon, F.: First observations of triple-frequency radar Doppler spectra in snowfall: Interpretation and applications, *Geophys. Res. Lett.*, 43, 2225–2233, <https://doi.org/10.1002/2015GL067618>, 2016.
- Kollias, P., Szyrmer, W., Rémillard, J., and Luke, E.: Cloud radar Doppler spectra in drizzling stratiform clouds: 2. Observations and microphysical modeling of drizzle evolution, *J. Geophys. Res.-Atmos.*, 116, D13203, <https://doi.org/10.1029/2010JD015238>, 2011.
- Korolev, A., Mcfarquhar, G., Field, P., Franklin, C., Lawson, P., Wang, Z., Williams, E., Abel, S., Axisa, D., Borrmann, S., Crosier, J., Fugal, J., Krämer, M., Lohmann, U., Schlenczek, O., and Wendisch, M.: Mixed-Phase Clouds: Progress and Challenges, *Meteor. Mon.*, 58, 5.1–5.50, <https://doi.org/10.1175/AMSMONOGRAPHS-D-17-0001.1>, 2017.
- Leinonen, J., Kneifel, S., and Hogan, R. J.: Evaluation of the Rayleigh–Gans approximation for microwave scattering by rimed snowflakes, *Q. J. Roy. Meteorol. Soc.*, 144, 77–88, <https://doi.org/10.1002/qj.3093>, 2018.
- Lu, Y., Jiang, Z., Aydin, K., Verlinde, J., Clothiaux, E. E., and Botta, G.: A polarimetric scattering database for non-spherical ice particles at microwave wavelengths, *Atmos. Meas. Tech.*, 9, 5119–5134, <https://doi.org/10.5194/amt-9-5119-2016>, 2016.
- Luke, E. P., Yang, F., Kollias, P., Vogelmann, A. M., and Maahn, M.: New insights into ice multiplication using remote-sensing observations of slightly supercooled mixed-phase clouds in the Arctic, *P. Natl. Acad. Sci. USA*, 118, e2021387118, <https://doi.org/10.1073/pnas.2021387118>, 2021.
- Löhnert, U., Schween, J. H., Acquistapace, C., Ebell, K., Maahn, M., Barrera-Verdejo, M., Hirsikko, A., Bohn, B., Knaps, A., O'Connor, E., Simmer, C., Wahner, A., and Crewell, S.: JOYCE: Jülich Observatory for Cloud Evolution, *B. Am. Meteorol. Soc.*, 96, 1157–1174, <https://doi.org/10.1175/BAMS-D-14-00105.1>, 2015.
- Madonna, F., Amodeo, A., D'Amico, G., and Pappalardo, G.: A study on the use of radar and lidar for characterizing ultragraining aerosol, *J. Geophys. Res.-Atmos.*, 118, 10056–10071, <https://doi.org/10.1002/jgrd.50789>, 2013.
- Mamouri, R.-E.: Custom collection of categorize, classification, drizzle, ice water content, and liquid water content data from Limassol between 19 Oct 2016 and 25 Mar 2018, ACTRIS Cloud remote sensing data centre unit (CLU), Cloudnet [data set], <https://hdl.handle.net/21.12132/2.a056a828a6b94d1f> (last access: 6 February 2024), 2021.
- Matrosov, S., Mace, G., Marchand, R., Shupe, M., Hallar, A., and McCubbin, I.: Observations of Ice Crystal Habits with a Scanning Polarimetric W-Band Radar at Slant Linear Depolariza-

- tion Ratio Mode, *J. Atmos. Ocean. Technol.*, 29, 989–1008, <https://doi.org/10.1175/JTECH-D-11-00131.1>, 2012.
- Matrosov, S. Y.: Prospects for the measurement of ice cloud particle shape and orientation with elliptically polarized radar signals, *Radio Sci.*, 26, 847–856, <https://doi.org/10.1029/91RS00965>, 1991.
- Matrosov, S. Y.: Polarimetric Radar Variables in Snowfall at Ka- and W-Band Frequency Bands: A Comparative Analysis, *J. Atmos. Ocean. Technol.*, 38, 91–101, <https://doi.org/10.1175/JTECH-D-20-0138.1>, 2021.
- Matrosov, S. Y., Reinking, R. F., Kropfli, R. A., Martner, B. E., and Bartram, B. W.: On the Use of Radar Depolarization Ratios for Estimating Shapes of Ice Hydrometeors in Winter Clouds, *J. Appl. Meteorol.*, 40, 479–490, [https://doi.org/10.1175/1520-0450\(2001\)040<0479:OTUORD>2.0.CO;2](https://doi.org/10.1175/1520-0450(2001)040<0479:OTUORD>2.0.CO;2), 2001.
- Matrosov, S. Y., Reinking, R. F., and Djalalova, I. V.: Inferring Fall Attitudes of Pristine Dendritic Crystals from Polarimetric Radar Data, *J. Atmos. Sci.*, 62, 241–250, <https://doi.org/10.1175/JAS-3356.1>, 2005.
- Morrison, H., de Boer, G., Feingold, G., Harrington, J., Shupe, M. D., and Sulia, K.: Resilience of persistent Arctic mixed-phase clouds, *Nat. Geosci.*, 5, 11–17, <https://doi.org/10.1038/ngeo1332>, 2012.
- Myagkov, A., Seifert, P., Wandinger, U., Bauer-Pfundstein, M., and Matrosov, S. Y.: Effects of Antenna Patterns on Cloud Radar Polarimetric Measurements, *J. Atmos. Ocean. Technol.*, 32, 1813–1828, <https://doi.org/10.1175/JTECH-D-15-0045.1>, 2015.
- Myagkov, A., Seifert, P., Bauer-Pfundstein, M., and Wandinger, U.: Cloud radar with hybrid mode towards estimation of shape and orientation of ice crystals, *Atmos. Meas. Tech.*, 9, 469–489, <https://doi.org/10.5194/amt-9-469-2016>, 2016a.
- Myagkov, A., Seifert, P., Wandinger, U., Bühl, J., and Engelmann, R.: Relationship between temperature and apparent shape of pristine ice crystals derived from polarimetric cloud radar observations during the ACCEPT campaign, *Atmos. Meas. Tech.*, 9, 3739–3754, <https://doi.org/10.5194/amt-9-3739-2016>, 2016b.
- Pruppacher, H. and Klett, J.: *Microphysics of Clouds and Precipitation*, Springer Dordrecht, Atmospheric and Oceanographic Sciences Library (ATSL), Vol. 18, Springer, <https://doi.org/10.1007/978-0-306-48100-0>, 1997.
- Radenz, M., Bühl, J., Seifert, P., Griesche, H., and Engelmann, R.: peakTree: a framework for structure-preserving radar Doppler spectra analysis, *Atmos. Meas. Tech.*, 12, 4813–4828, <https://doi.org/10.5194/amt-12-4813-2019>, 2019.
- Radenz, M., Bühl, J., Seifert, P., Baars, H., Engelmann, R., Barja González, B., Mamouri, R.-E., Zamorano, F., and Ansmann, A.: Hemispheric contrasts in ice formation in stratiform mixed-phase clouds: disentangling the role of aerosol and dynamics with ground-based remote sensing, *Atmos. Chem. Phys.*, 21, 17969–17994, <https://doi.org/10.5194/acp-21-17969-2021>, 2021.
- Reinking, R. F., Matrosov, S. Y., Kropfli, R. A., and Bartram, B. W.: Evaluation of a 45° Slant Quasi-Linear Radar Polarization State for Distinguishing Drizzle Droplets, Pristine Ice Crystals, and Less Regular Ice Particles, *J. Atmos. Ocean. Technol.*, 19, 296–321, <https://doi.org/10.1175/1520-0426-19.3.296>, 2002.
- Ryzhkov, A. V.: Interpretation of Polarimetric Radar Covariance Matrix for Meteorological Scatterers: Theoretical Analysis, *J. Atmos. Ocean. Technol.*, 18, 315–328, [https://doi.org/10.1175/1520-0426\(2001\)018<0315:IOPRCM>2.0.CO;2](https://doi.org/10.1175/1520-0426(2001)018<0315:IOPRCM>2.0.CO;2), 2001.
- Schimmel, W., Kalesse-Los, H., Maahn, M., Vogl, T., Foth, A., Garfias, P. S., and Seifert, P.: Identifying cloud droplets beyond lidar attenuation from vertically pointing cloud radar observations using artificial neural networks, *Atmos. Meas. Tech.*, 15, 5343–5366, <https://doi.org/10.5194/amt-15-5343-2022>, 2022.
- Solomon, A., de Boer, G., Creamean, J. M., McComiskey, A., Shupe, M. D., Maahn, M., and Cox, C.: The relative impact of cloud condensation nuclei and ice nucleating particle concentrations on phase partitioning in Arctic mixed-phase stratocumulus clouds, *Atmos. Chem. Phys.*, 18, 17047–17059, <https://doi.org/10.5194/acp-18-17047-2018>, 2018.
- Tetoni, E., Ewald, F., Hagen, M., Köcher, G., Zinner, T., and Groß, S.: Retrievals of ice microphysical properties using dual-wavelength polarimetric radar observations during stratiform precipitation events, *Atmos. Meas. Tech.*, 15, 3969–3999, <https://doi.org/10.5194/amt-15-3969-2022>, 2022.
- Vogl, T., Maahn, M., Kneifel, S., Schimmel, W., Moisseev, D., and Kalesse-Los, H.: Using artificial neural networks to predict riming from Doppler cloud radar observations, *Atmos. Meas. Tech.*, 15, 365–381, <https://doi.org/10.5194/amt-15-365-2022>, 2022.
- von Terzi, L., Dias Neto, J., Ori, D., Myagkov, A., and Kneifel, S.: Ice microphysical processes in the dendritic growth layer: a statistical analysis combining multi-frequency and polarimetric Doppler cloud radar observations, *Atmos. Chem. Phys.*, 22, 11795–11821, <https://doi.org/10.5194/acp-22-11795-2022>, 2022.
- Welss, J.-N., Siewert, C., and Seifert, A.: Explicit habit-prediction in the Lagrangian super-particle ice microphysics model McSnow, ESS Open Archive eprints, 180, [essoar.168614461.18006193/v1](https://doi.org/10.22541/essoar.168614461.18006193/v1), 2023.